# An integrated workflow for stress and flow modelling using outcrop-derived discrete fracture networks

Bisdom, K.; Nick, H. M.; Bertotti, G.

**DOI**
10.1016/j.cageo.2017.02.019

**Publication date**
2017

**Document Version**
Accepted author manuscript

**Published in**
Computers & Geosciences: an international journal

**Citation (APA)**
Bisdom, K., Nick, H. M., & Bertotti, G. (2017). An integrated workflow for stress and flow modelling using outcrop-derived discrete fracture networks. *Computers & Geosciences: an international journal*, *103*, 21-35. https://doi.org/10.1016/j.cageo.2017.02.019

Postprint of Computers & Geosciences: an international journal
Volume 103, June 2017, Pages 21–35
Link to formal publication (Elsevier): http://dx.doi.org/10.1016/j.cageo.2017.02.019

# An integrated workflow for stress and flow modelling using outcrop-derived discrete fracture networks

K. Bisdom[1], H. M. Nick[1,2], G. Bertotti[1]

1) Department of Geoscience & Engineering, Delft University of Technology, Delft, Netherlands

2) The Danish Hydrocarbon Research and Technology Centre, Technical University of Denmark, Copenhagen, Denmark

Keywords: permeability tensor; discrete fracture matrix; aperture; fracture permeability; fracture networks; fracture mechanics; outcrop analogue modelling; Brazil

## Abstract

Fluid flow in naturally fractured reservoirs is often controlled by subseismic-scale fracture networks. Although the fracture network can be partly sampled in the direct vicinity of wells, the inter-well scale network is poorly constrained in fractured reservoir models. Outcrop analogues can provide data for population of domains of the reservoir model where no direct measurements are available. However, extracting relevant statistics from large outcrops representative of inter-well scale fracture networks remains challenging. Recent advances in outcrop imaging provide high-resolution datasets that can cover areas of several hundred by several hundred meters, i.e. the domain between adjacent wells, but even then, data from the

high-resolution models is often upscaled to reservoir flow grids, resulting in loss of accuracy. We present a workflow that uses photorealistic georeferenced outcrop models to construct geomechanical and fluid flow models containing thousands of discrete fractures covering sufficiently large areas, that does not require upscaling to model permeability. This workflow seamlessly integrates geomechanical Finite Element models with flow models that take into account stress-sensitive fracture permeability and matrix flow to determine the full permeability tensor. The applicability of this workflow is illustrated using an outcropping carbonate pavement in the Potiguar basin in Brazil, from which 1082 fractures are digitised. The permeability tensor for a range of matrix permeabilities shows that conventional upscaling to effective grid properties leads to potential underestimation of the true permeability and the orientation of principal permeabilities. The presented workflow yields the full permeability tensor model of discrete fracture networks with stress-induced apertures, instead of relying on effective properties as most conventional flow models do.

# 1. Introduction

Natural fracture networks are multiscale systems that develop through a combination of mechanisms that are only partly understood (Olson et al., 2009; Philip et al., 2005). Understanding the multiscale distribution of fracture networks in the subsurface allows for optimisation of fractured reservoir development (Nelson, 2001). However, limited observations from seismic and wells do not provide the complete fracture network geometry and associated flow properties, particularly of the subseismic fracture network (Fabuel-Perez et al., 2010; Martinez-Landa et al., 2016). Outcrops are the only source to obtain realistic descriptions of fracture networks, as no models exist that can create realistic fracture networks on the scale of fractured reservoirs. To derive lessons for fractured reservoirs, we need outcropping datasets that contain at least several hundred fractures covering several orders of magnitude in spacing and length, without suffering from censoring and truncation

52 artefacts, over an area that covers at least several grid blocks in conventional reservoir flow
53 models (Bonnet et al., 2001; Ortega et al., 2006). Such datasets are not easily obtained from
54 conventional outcrop photographs or scanline studies, as these methods capture only a limited
55 number of scales (Bisdom et al., 2014).

56 Photogrammetry, particularly Structure from Motion (SfM) Multiview stereo (MVS),
57 is an inexpensive and fast method to accurately map 3-D structures from 2-D images taken
58 from different positions (Harwin and Lucieer, 2012; Ullman, 1979). In recent years, this
59 method has been embraced by geologists to create digital outcrop models as an alternative to
60 the more expensive and less flexible LiDAR (Light Image Detection And Ranging) methods
61 (Hodgetts, 2013; Mahmud et al., 2015; Reif et al., 2011; Rotevatn et al., 2009; Tavani et al.,
62 2014; Wilson et al., 2011). Partly overlapping images are aligned by identifying and
63 extracting common points, which can be positioned in 3-D space to reconstruct the outcrop
64 geometry (Bemis et al., 2014; James and Robson, 2012). The resulting models provide a
65 complete and unobstructed viewpoint of the outcrop that can be changed and adjusted for any
66 purpose (Tavani et al., 2016).

67 As this approach requires that the outcrop is fully covered by images with an overlap
68 of at least 50%, Unmanned Aerial Vehicles (UAVs or drones), equipped with a camera and
69 positioning sensors, are best suited to acquire the images required for photogrammetry
70 modelling (e.g. Bemis et al., 2014; Bond et al., 2015; Hodgetts, 2013; James and Robson,
71 2012; Tavani et al., 2014; Vasuki et al., 2014; Vollgger and Cruden, 2016). Fracture
72 geometries can be extracted from the resulting georeferenced models in 2-D or 3-D (Duelis
73 Viana et al., 2016; Hardebol and Bertotti, 2013; Tavani et al., 2014). Extraction of 2-D data
74 from a 3-D photogrammetry model is more accurate than fracture interpretation from
75 conventional 2-D images, as the photogrammetry model is accurately orthorectified and the
76 multiple viewpoints allow for more precise digitisation of fracture geometry. Irrespective of

whether the fracture data is used for 2-D or 3-D analysis, 3-D outcrop models provide a higher accuracy.

The second challenge is to obtain realistic aperture predictions from outcropping geometries. At depth, permeability is a function of aperture, which is partly controlled by the in-situ stresses (Baghbanan and Jing, 2008; Lei et al., 2015; Tao et al., 2009; Zoback, 2007), but pressure relief during exhumation and weathering dissolves cements and changes aperture. Outcropping apertures are therefore not representative, unless it can be proven that fractures have not been reactivated during exhumation. This is typically assumed to be the case for veins (e.g. Hooker et al., 2014), but preserved veins are relatively rare. Alternatively, aperture is modelled as a function of stress, using subcritical crack growth as defined by Linear Elastic Fracture Mechanics (LEFM) or conductive shearing defined by Barton-Bandis (Barton, 1982; Barton et al., 1985; Barton and Bandis, 1980; Lawn and Wilshaw, 1975; Olson, 2003; Pollard and Segall, 1987; Vermilye and Scholz, 1995). These models require the local stress state, which is typically derived from Finite Element (FE) models with explicit fracture representations (Barton, 2014; Bisdom et al., 2016b; Lei et al., 2016, 2014; Nick et al., 2011).

The third challenge is modelling permeability through fractured rocks, taking into account the coupled flow through fractures and matrix (Belayneh et al., 2009; Geiger et al., 2013; Lang et al., 2014). Conventional reservoir simulation tools scale up fracture density, porosity and permeability to effective grid properties in dual-porosity dual-permeability grids, resulting in a significantly simplified flow model (Cottereau et al., 2010; Geiger and Matthäi, 2012; Jonoud and Jackson, 2008). Methods exist to model flow through discrete fracture-matrix models without requiring upscaling, making use of a Finite-Element Finite-Volume (FE-FV) approach, but the use of these methods is often limited to relatively small-scale synthetic fracture networks (Lei et al., 2014; Matthäi and Belayneh, 2004).

These individual problems have been studied extensively, focusing on 3-D outcrop modelling (Hodgetts, 2013; Tavani et al., 2014; Vasuki et al., 2014), meshing (Karimi-Fard and Durlofsky, 2016; Nejati et al., 2016; Nick and Matthäi, 2011a; Paluszny et al., 2007) and flow modelling (Lang et al., 2014; Nick and Matthäi, 2011b), but integrating these components remains a challenge. Our aim is to present an integrated workflow for modelling the complete permeability tensor of large-scale fracture networks with apertures representative of in-situ stress conditions by combining fast data acquisition using a UAV with outcrop modelling using photogrammetry (Figure 1). This workflow builds upon the stress-aperture modelling approach presented in Bisdom et al. (2016b), making use of the geometrical aperture approximation from Bisdom et al. (2016d), and the modelling of permeability for a range of aperture definitions presented in (Bisdom et al., 2016d). The 3-D outcrop models are used to accurately digitise fracture patterns in 2-D, which form the basis for stress, aperture and equivalent permeability (i.e. combined matrix and fracture permeability) models. The main result is a discrete fracture-matrix model consisting of an unstructured mesh with discrete fractures, from which the full permeability tensor is calculated. The aim of this workflow is to improve the representativeness of outcrops as a proxy for flow in naturally fractured reservoirs, by capturing larger-scale high-resolution fracture patterns covering distances comparable to well spacing in fractured reservoirs, followed by modelling of aperture and flow representative of subsurface conditions. We illustrate the effectiveness of the workflow using an example of 2-D fracture patterns in outcropping carbonates in the Potiguar Basin, NE Brazil (Bertotti et al., **accepted**; de Graaf et al., 2017).

# 2. Quantitative outcrop modelling using a UAV and photogrammetry

## *2.1. Image acquisition with a UAV*

We use a multi-rotor UAV (Figure 2) to acquire images of multiscale fracture patterns over an area that covers several reservoir simulation grid blocks, which are subsequently merged into 2-D georeferenced outcrop models. To ensure that an area is fully covered by images with constant overlap, flight paths are programmed prior to flights (Figure 3). The programmed flights are automatically executed and controlled using a GNSS sensor (2 m accuracy) for horizontal positioning and a temperature-compensated barometer (dm-accuracy) for vertical positioning. A magnetic compass provides the absolute heading and accelerometers and a gyroscope further control the position of the UAV and ensure stable operation. Flight and environment conditions are continuously monitored and stored during flights for quality-check and diagnostic purposes.

Outcrop images are taken with a 14-megapixel compact camera in a motorised mount attached to the UAV. The resulting image resolution depends on the altitude and camera specifications. A distance of 50 m between the UAV and the surface of interest yields a resolution $R$ of 1.44 cm/px, which changes linearly with changing distance $H$ (in m):

$$R = \frac{100 w_s H}{w_i F_r} \quad , \tag{1.1}$$

where $w_s$ is the camera sensor width (in mm), $w_i$ is the image width (in pixels) and $F_r$ is the real focal length (in mm) for the focal length in a 35 mm equivalent (*F35*):

$$F_r = \frac{F_{35} w_s}{34.6} \quad . \tag{1.2}$$

Depending on outcrop size and required resolution, most flights are between 20-100 m altitude, corresponding to resolutions of 0.6-2.9 cm/px respectively. For each image, the corresponding UAV position (horizontal coordinates and altitude) and orientation are determined using the GNSS sensor and barometer. To further constrain the outcrop position, brightly marked GCPs (Ground Control Points) are positioned on the outcrop surface, which are georeferenced with a GPS, and we measure the distance between these points using a hand-held laser range finder for further scaling of the model.

### *2.2. Outcrop model construction using photogrammetry*

Using Agisoft PhotoScan®, we process the UAV images and location data into georeferenced 2-D and 3-D outcrop models. This workflow consists of image alignment, point cloud generation, surface meshing and texturing (Figure 4 and Figure 5).

#### *2.2.1. Image alignment*

The approximate position from where each image is taken, is used to identify the image pairs that are likely to overlap. Common points are identified and extracted and positioned in 3-D in a *sparse point cloud* (Figure 4a). The vertical position of a point is determined from the relative change in position in the partly overlapping images, where one point is imaged from different angles.

#### *2.2.2. Point cloud generation*

Once images are aligned, all points from the aligned images are extracted and positioned in 3-D to generate a *dense point cloud* (Figure 4b and Figure 5a). Depending on flight altitude, the point cloud can have a resolution that is similar to LiDAR datasets. A single flight at 50 m altitude, capturing 100 images covering an area of 200 m × 200 m, results in a dense point cloud of $1.4 \times 10^7$ points (35 points per $m^2$; Figure 4b). Higher-detail models, for example

captured from an altitude of 3m, yield point clouds of $8.6\times10^7$ points for an area of 20 m × 30 m ($1.4\times10^4$ points per $m^2$; Figure 5a).

When the images are georeferenced, aligning and dense point cloud generation are relatively fast processes that can be completed during a fieldwork campaign, providing an almost immediate data check to analyse whether data acquisition was successful or additional flights are required. Furthermore, having already a high-resolution point cloud in the field can be useful in identifying interesting features or sections of the outcrop that warrant further inspection, or additional higher-resolution flights.

### *2.2.3. Surface generation*

Interpretation of outcropping features requires converting the point cloud into a meshed surface consisting of triangulated elements (Figure 5). The meshed surface can have the same resolution as the dense point cloud, but for sub-horizontal pavements a downsampled mesh is typically sufficient. For this example, the point cloud consists of $8.6\times10^7$ points whereas the resulting surface is downsampled to $2\times10^6$ elements (Figure 5b,c). This surface has a sufficiently high resolution for 2-D fracture interpretation. After surface generation, the outcrop model can be exported as a 3-D textured geometry to geological modelling software or as 2-D georeferenced orthomosaic images to GIS-based software.

## *2.3. Fracture digitisation*

Fractures in the 2-D orthomosaic images are digitised in GIS-tools such as DigiFract (Hardebol and Bertotti, 2013). Fracture lengths are manually traced, and attributes including orientation and infill can be assigned. Manual interpretation is time-intensive, but automatic tracking methods are not sufficiently sophisticated to replace manual interpretation, and require time-intensive quality-checking and manual corrections (Duelis Viana et al., 2016; Lin et al., 2015; Vasuki et al., 2014).

After digitisation, orientation, spacing and length distributions are calculated (Figure 6). Length or height is plotted using frequency distributions (Figure 6c,d). The orientation distribution is visualised using rose diagrams or stereoplots (Figure 6b). Fracture spacing is calculated using a combination of methods, where $P_{10}$ intensity, which is the 1-D fracture density measured along a line (Dershowitz, 1985), is calculated using a large amount of closely-spaced scanlines, which are projected along the entire height or length of an outcrop (Hardebol and Bertotti, 2013). Alternatively, spacing is defined by $P_{21}$ intensity, which is the total fracture length versus outcrop area (Dershowitz, 1985), calculated by summing the total length or height of fractures within the entire outcrop or in individual beds as a function of outcrop area (Wu and Pollard, 2002). The $P_{21}$ method is sensitive to boundary effects, as the length of fractures that intersect the boundary cannot be fully quantified, resulting in a potential underestimation of length (Mauldon, 1998; Pahl, 1981; Zhang and Einstein, 1998). Using circular sampling windows and correction methods, this can be compensated for (Mauldon et al., 2001), but alternatively fractures that intersect the sampling boundary can be identified and excluded from the length analysis entirely.

The full spacing distribution is analysed using box-counting methods (Bonnet et al., 2001), where the outcrop is either divided into boxes with a constant area, in which $P_{21}$ intensity is calculated (Figure 6e), or the $P_{21}$ intensity is calculated within a circle with a fixed centre and an increasing radius (Bonnet et al., 2001; Reith, 2015). The latter method also provides a means for characterising the Representative Elementary Area (REA), which is an indication for the optimal grid cell size for upscaled fracture flow modelling (Dershowitz and Doe, 1997; Long and Witherspoon, 1985). These methods help to identify whether the digitised networks follow power-law scaling trends (Bonnet et al., 2001; Bour and Davy, 1997; Davy et al., 1990).

The size and spacing distributions are corrected for censoring artefacts, which result from fractures that are not fully captured in the model such that their true length or height is unknown (Bonnet et al., 2001; Ortega et al., 2006). We correct for this by filtering all fractures that intersect the user-defined outcrop boundaries and by manually identifying and excluding areas obscured by for example trees. Truncation artefacts, which are related to the resolution limit of the outcrop model such that the smallest fractures are typically under-represented, cannot be corrected automatically. Truncated length and spacing scales need to be identified by the user, based on the image resolution limit.

# 3. Finite Element meshing and stress modelling

The 2-D fracture networks are meshed for mechanical and flow modelling, using unstructured FE meshes with explicit fractures. The meshing and the subsequent geomechanical simulations are done using ABAQUS CAE® (Dassault Systèmes®). Compared to other meshing tools, we find that this tool can handle meshing of more complex geometries, with minimal pre- and postprocessing.

## *3.1. Meshing of discrete fractures*

Accurate representation of fracture connectivity and topology is essential, particularly when the matrix is close to impermeable (Figure 7) (Hardebol et al., 2015; Sanderson and Nixon, 2015). To ensure that fracture connections and intersections are correct, most GIS tools have manual or automatic snapping options that can be used. The topology is converted to a CAD file that forms the basis for the FE model. To avoid boundary effects, rectangular model boundaries are used with an intact rock buffer zone between the fracture network and model boundary (Figure 8). The model is meshed using quadratic plane strain elements, with refinements along the fractures (Figure 9). To avoid singularity issues, we further refine the mesh around fracture tips. To model fracture opening and closing, fractures are represented

as seams in the mesh, using a set of post-processing functions written in Python that update the mesh to generate seams (Figure 10). A seam is generated by duplicating nodes along a seam and splitting the mesh (Figure 11). The individual seams are generated sequentially, taking into account existing seams. Except for the intersecting seams, the output mesh is identical to the input mesh, and can be read directly into the FE simulator for analysis of the stress distribution in a complex fracture network.

### *3.2. Geomechanical FE model set-up*

Using the ABAQUS Implicit solver, the local stress state is modelled, from which fracture apertures can be derived using stress-aperture relations (Bisdom et al., 2016b). These models take into account a far-field differential stress applied to the boundaries as pressure loads (Figure 8). Maximum and minimum principle stresses are applied perpendicular to the model boundaries in a stress initialisation step, during which movement of fracture planes and boundaries is constrained. After successful stress initialisation, the displacement conditions are released to let the model equilibrate (Figure 8), solving for the stress tensor $\boldsymbol{\sigma}$ in fully elastic rocks (Nick et al., 2011):

$$\boldsymbol{\sigma} = \boldsymbol{D}_C \left( \boldsymbol{\varepsilon} - \boldsymbol{\varepsilon}_0 \right) + \boldsymbol{\sigma}_0 , \tag{1.3}$$

where $\boldsymbol{\varepsilon}$ and $\boldsymbol{\varepsilon_0}$ are the strain and initial strain vectors, $\boldsymbol{\sigma_0}$ is the initial stress vector and $\boldsymbol{D_C}$ is the material stiffness matrix:

$$\boldsymbol{D}_C = \frac{E}{(1+\nu)(1-2\nu)} \begin{bmatrix} 1-\nu & \nu & 0 \\ \nu & 1-\nu & 0 \\ 0 & 0 & 1-2\nu \end{bmatrix}, \tag{1.4}$$

with Young's modulus $E$ and Poisson's ratio $\nu$.

The slip tendency of fractures can be defined by a linear Mohr-Coulomb friction coefficient or non-linear behaviour, e.g. Barton-Bandis conductive shearing (Bisdom et al.,

2016b), which can be defined by functions or look-up tables. A heterogeneous or constant pore pressure distribution can also be taken into account, as well as single-phase flow injection to take into account localised changes in pore pressure over time (Bisdom et al., 2016a).

### *3.3. Aperture modelling*

For each fracture node, stress-dependent apertures are calculated from the local normal and shear stresses in the geomechanical FE model (Figure 12). Different stress-aperture relations can be used to calculate the corresponding spatial aperture distribution, capturing small-scale variations along individual fractures (Appendix A; Bisdom et al., 2016d). Aperture definitions that are not a function of stress, such as power-law scaling, are calculated using *Python* functions in a GIS environment, where aperture is calculated for each fracture segment based on the geometrical properties of that segment. Using the *x*,*y*-positions, these values are translated from the segments to the nodes of the mesh (Bisdom et al., 2016c, 2016d). Four commonly-used aperture definitions have been implemented into the workflow, but other definitions can be easily added. These definitions are (sub-)linear length aperture scaling predicted by LEFM, power-law scaling and Barton-Bandis conductive shearing derived from either FE models or geometrical approximations (Appendix A).

## 4. Flow modelling

To construct the flow model, we use the workflow from (Bisdom et al., 2016b) summarised below. Here, we extend this workflow from calculating only equivalent permeability parallel to the edges of the model to calculating the full permeability tensor to derive the principal maximum and minimum permeability values.

Flow is modelled using the same FE mesh used for the geomechanical models, where the seams in the mesh have been replaced by lower-dimensional elements to which modelled

fracture apertures are assigned (Bisdom et al., 2016b). In addition, the buffer zone added to avoid stress boundary effects is removed such that fractures intersect the edges of the model. We use a hybrid Finite-Element Finite-Volume (FE-FV) approach implemented in the Complex Systems Modelling Platform to solve the flow equations (Matthäi et al., 2007).

Similar to Durlofsky (1991), the full equivalent permeability tensor (**k**) is computed by solving the steady state continuity equation for flow in different directions using a far-field pressure gradient applied in both horizontal directions of the rectangular 2-D pavements. Note that the superscripts 1 and 2 are used for these two problems in Eq. (1.5) and a constant viscosity ($\mu$) is assumed. This is followed by volume-averaging (for both problems $\langle\,\rangle^1$, $\langle\,\rangle^2$) of resulted fluid velocities ($u_x$ and $u_y$) and pressure gradients ($\nabla p_x$, $\nabla p_y$) to solve for equivalent tensor permeability through:

$$\langle \nabla p \rangle \mathbf{k} = -\mu \langle u \rangle \Rightarrow \begin{bmatrix} \langle \nabla p_x \rangle^1 & \langle \nabla p_y \rangle^1 & 0 & 0 \\ 0 & 0 & \langle \nabla p_x \rangle^1 & \langle \nabla p_y \rangle^1 \\ \langle \nabla p_x \rangle^2 & \langle \nabla p_y \rangle^2 & 0 & 0 \\ 0 & 0 & \langle \nabla p_x \rangle^2 & \langle \nabla p_y \rangle^2 \\ 0 & 1 & -1 & 0 \end{bmatrix} \begin{Bmatrix} k_{xx} \\ k_{xy} \\ k_{yx} \\ k_{yy} \end{Bmatrix} = -\mu \begin{Bmatrix} \langle u_x \rangle^1 \\ \langle u_y \rangle^1 \\ \langle u_x \rangle^2 \\ \langle u_y \rangle^2 \\ 0 \end{Bmatrix}. \quad (1.5)$$

The maximum and minimum principal permeability values ($k_{max}$, $k_{min}$) as well as the principal direction ($\theta$) can be calculated.

## 5. Application

The integrated workflow is applied to model permeability through an outcropping network of fractures in the Jandaíra Formation, which is a carbonate formation that crops out in large parts of the Potiguar Basin in NE Brazil. Extensive fracture networks were formed predominantly during burial in a compressional setting (Bertotti et al., **accepted**; de Graaf et

al., 2017). The sub-horizontal position of the rocks provides excellent exposures of multiscale fracture patterns covering areas of several hundred by several hundred meters, which is comparable to the spacing of wells in a fractured reservoir (Bisdom et al., **accepted**). In conventional reservoir models, these areas are typically populated with stochastic fractures whose distributions are derived from well data or small outcrops. We use our workflow to capture and create a deterministic discrete fracture flow model, focusing on a rectangular area of a pavement in the western part of the basin in which there is a minimal impact of censoring caused by a few trees (Figure 13). This study area is ideal for 2-D geomechanical and flow analysis, as all fractures dip perpendicular to the sub-horizontal bedding planes (Bisdom et al., **accepted**). Hence, spacings and lengths interpreted on the pavements do not require any Terzaghi corrections, and the complete orientation distribution can be quantified by digitising fracture strikes. Geometrical analysis of fractures in the Potiguar basin is outside the scope of this work, but presented elsewhere (Bertotti et al., **accepted**; Bisdom et al., **accepted**; de Graaf et al., 2017).

### *5.1. Fracture network geometry*

The area of interest was imaged with the UAV at an altitude of 50 m above the ground, resulting in 90 images with a resolution of 1.44 cm/px. The model was accurately georeferenced using several GCPs, for which we measured the absolute position and the distance between the GCPs. The resulting dense point cloud covers an area of $4.1\times10^4$ $m^2$ with a point density of 284 $m^{-1}$. The georeferenced orthomosaic has the same resolution as the individual images (1.44 cm/px; Figure 13). Using DigiFract, we digitised 1082 fractures in a rectangular area of 150 m × 142 m (Figure 14b). Three orientation families were identified with size and spacing distributions that follow power-law scaling trends (Bisdom et al., **accepted**). Weathering has affected apertures and limits the view of the smallest fracture scales (i.e. smaller than 1 m), but these smaller length scales have only a relatively small

impact on permeability compared to the large connected system of fractures. Recent weathering also created dendritic dissolution patterns, which are excluded from the analysis.

### 5.2. *Fracture aperture distribution*

Most fractures are open and free from cement, i.e. barren, but this is associated with exhumation and weathering (Bertotti et al., **accepted**). To define apertures representative of subsurface conditions, we use a sublinear length-aperture scaling model defined by Linear Elastic Fracture Mechanics (LEFM; Atkinson, 1984; Bisdom et al., 2016c; Lawn and Wilshaw, 1975; Olson, 2003). The far-field stress is defined by a 30 MPa $\sigma_1$ applied as pressure loads perpendicular to the north and south boundaries and a $\sigma_3$ of 10 MPa oriented E-W. These stress directions are comparable to the paleostress directions under which most of the fractures were formed (Bertotti et al., **accepted**). In the absence of measurements of the elastic rock properties, the rock is assumed fully elastic with a Poisson's ratio of 0.3 and a Young's modulus of 50 GPa. The model mesh consists of $5.1\times10^5$ triangulated elements (Figure 14a).

The resulting aperture scales with length and stress (Figure 14b). Aperture follows a lognormal distribution with a maximum of 2.5 mm and an average of 0.5 mm. One percent of fractures is hydraulically closed, but the majority of the network is permeable (Figure 14c,d).

### 5.3. *Equivalent permeability*

For a 1 mD matrix, the pressure gradient in the *x*- and *y*-directions is highly heterogeneous, particularly in the *x*-direction (Figure 14c,d). We quantify permeability as the ratio between equivalent and matrix permeability, which quantifies the contrast between matrix and fractures (Figure 15). The ratio is high for a low matrix permeability, as most flow is carried by the fractures, and decreases for increasing matrix permeability. For a low permeability

matrix (1 mD), fracture flow in the *y*-direction is more dominant than the *x*-direction (Figure 15a,b), but remarkably this is reversed for higher matrix permeabilities (Figure 15c,d).

This reversal is better quantified using the fluid velocities, which show that one large fracture percolates through the entire model in the *y*-direction, creating a flow pathway even when matrix permeability is low (Figure 15a,b). There are several large E-W striking fractures with large apertures, but they do not fully percolate the model, limiting their impact in a low-permeability matrix.

This change in permeability is better explained by calculating the full permeability tensor (Figure 16). For matrix permeabilities below 100 mD, maximum permeability is in a NE-SW direction. In this domain, permeability is controlled by fracture flow. For increasing matrix permeability, flow is carried by a mix of fractures and matrix, and the maximum permeability rotates to ENE-WSW, remaining anisotropic. Only when matrix permeability is larger than several Darcy, flow is fully carried by the matrix and permeability becomes isotropic. However, for most models, the highly-connected high-intensity fracture network controls flow either completely or partly.

# 6. Discussion

## *6.1. From outcrops to representative subsurface flow models*

Contrary to other studies, the presented workflow uses only the outcropping network geometry as input for deterministic flow models, not taking into account outcropping apertures. Instead, we use geomechanical FE models to solve the stress state around the fracture network, based on estimates of subsurface stress conditions and rock properties. These geomechanical parameters can typically be derived from subsurface datasets, albeit with uncertainty ranges. However, the applied methodology is fast, allowing the inclusion of uncertainty ranges. The resulting stress states are used to calculate aperture, using different

377 stress-aperture relations (Bisdom et al., 2016d). This combination of outcropping geometries
378 and subsurface stress states and aperture distributions results in models that are more
379 representative of fractured reservoir permeability compared to analogue studies that use
380 apertures of exhumed barren fractures or assume a constant aperture for the entire network
381 (Makedonska et al., 2016).

382 Laser scanning of outcrops is an alternative method that provides deterministic
383 representations of entire outcrops, but photogrammetry offers more flexibility (Hodgetts,
384 2013). Through the use of deterministic 2-D patterns rather than stochastic fracture networks
385 derived from 1-D distributions, more realistic estimates of permeability can be made.
386 Stochastic models typically contain mutually crosscutting networks of fractures resulting in
387 highly connected networks with consistently high permeabilities, which does not correspond
388 to observations of permeability heterogeneity typically observed in fractured reservoirs. The
389 studied deterministic pattern better represents natural fracture topology with terminating
390 rather than fully crosscutting fractures (Hardebol et al., 2015; Sanderson and Nixon, 2015).

391 ### *6.2. Lessons for reservoir-scale flow modelling*

392 The studied fracture network from the Potiguar basin contains predominantly N-S and E-W
393 striking fractures that form an orthogonal pattern. Orthogonal patterns are observed in many
394 fractured outcrops and are assumed to be present in many subsurface reservoirs (Bai et al.,
395 2002). In reservoir-scale flow models, these patterns are upscaled to effective properties in
396 the two dominant fracture directions that are assumed to be representative of fracture
397 permeability, comparable to the equivalent permeability in the *x*- and *y*-directions. However,
398 by only considering flow in two directions, permeability is underestimated in this example, as
399 for a 1 mD matrix permeability, the permeability ratio in *x*- and *y*-directions is $1.9\times10^3$ and
400 $2.2\times10^3$ respectively, whereas the maximum ratio is $3.9\times10^3$ in the NE-SW direction. Even
401 for these relatively homogeneous orthogonal networks, the absolute maximum permeability

cannot be accurately determined using conventional upscaling. The outcrop-derived 2-D permeability tensor models can be used to determine the principal permeabilities of discrete fracture networks covering several grid cells, as a more accurate alternative to quantify permeability compared to ODA upscaling (Oda, 1985). These flow models also help to identify different fracture-matrix permeability domains, which can be used to better characterise fractured reservoir flow domains. To further bridge the gap between discrete fracture models and reservoir-scale continuum models, hybrid upscaling techniques can be used (Egya et al., 2016; Shah et al., 2016).

## 7. Conclusions

Outcrops provide a wealth of data for studying and modelling of fracture networks, which cannot be fully captured with 1-D scanlines, as these only capture spacing and aperture of one orientation set. LiDAR on the other hand captures entire outcrops at a high resolution, but this method has limited flexibility in terms of the type of outcrops it can be applied to and in terms of processing (Hodgetts, 2013). The presented workflow enables fast generation of highly detailed realistic fracture networks for use of geomechanical and flow modelling, variations of which have been applied to study different aspects of fracture and fracture-matrix flow (e.g. Aljuboori et al., 2015; Arnold et al., 2016; Bisdom et al., 2016c; Egya et al., 2016; Muhammad, 2016; Shah et al., 2016).

We use fracture patterns derived from these models for geomechanical and flow modelling of discrete fractures on a scale that is representative of part of a fractured reservoir, spanning an area of several conventional reservoir grid cells. The geomechanical model solves the local stress state within the fracture network, which is used to model aperture using a range of stress-aperture relations. The flow models consider matrix and fracture flow. Although the fluid pressure in the $x$- and $y$-directions of these models can be used to quantify

relative permeability differences between different models, it is not representative of the true principal permeabilities, even in an orthogonal network where fractures strike mainly parallel to the *x*- and *y*-directions. The presented workflow allows for fast quantification of the full permeability tensor in domains covering several conventional simulator grid cells using realistic fracture patterns digitised from outcrops, with minimal pre-processing and no upscaling.

## Acknowledgements

Total S.A. is thanked for sponsoring the PhD of the first author. The fracture patterns from the Potiguar basin were acquired with financial support from the National Petroleum Agency (ANP) of Brazil and Petrobras and with support in the field from numerous students from the VU University and Delft University of Technology in the Netherlands and F.H. Bezerra and his students from the Federal University of Rio Grande Do Norte (UFRN) in Brazil. The fracture data from Tunisia has been acquired with support from S. Bouaziz and A. Hammami from ENIS in Sfax, Tunisia. We thank N.J. Hardebol from Delft University of Technology and W. van der Zee and M. Holland from Baker Hughes for fruitful discussions and support regarding the geomechanical modelling, and S. Geiger for his input regarding flow modelling. We thank editor Gregoire Mariethoz, Andrea Billi and four anonymous reviewers for their suggestions to improve the earlier version of this manuscript.

## References

Aljuboori, F., Corbett, P., Bisdom, K., Bertotti, G., Geiger, S., 2015. Using Outcrop Data for Geological Well Test Modelling in Fractured Reservoirs, in: 77th EAGE Conference and Exhibition 2015. doi:10.3997/2214-4609.201413037

Arnold, D., Demyanov, V., Christie, M., Bakay, A., Gopa, K., 2016. Optimisation of decision

making under uncertainty throughout field lifetime: A fractured reservoir example. Comput. Geosci. 95, 123–139. doi:10.1016/j.cageo.2016.07.011

Atkinson, B.K., 1984. Subcritical crack growth in geological materials. J. Geophys. Res. 89, 4077. doi:10.1029/JB089iB06p04077

Baghbanan, A., Jing, L., 2008. Stress effects on permeability in a fractured rock mass with correlated fracture length and aperture. Int. J. Rock Mech. Min. Sci. 45, 1320–1334. doi:10.1016/j.ijrmms.2008.01.015

Bai, T., Maerten, L., Gross, M.R., Aydin, A., 2002. Orthogonal cross joints: do they imply a regional stress rotation? J. Struct. Geol. 24, 77–88. doi:10.1016/S0191-8141(01)00050-5

Bandis, S., 1980. Experimental Studies of Scale Effects on Shear Strength and Deformation of Rock Joints. University of Leeds. doi:10.12681/eadd/4686

Bandis, S.C., Lumsden, a. C., Barton, N.R., 1983. Fundamentals of rock joint deformation. Int. J. Rock Mech. Min. Sci. Geomech. Abstr. 20, 249–268. doi:10.1016/0148-9062(83)90595-8

Barton, N., 2014. Non-linear behaviour for naturally fractured carbonates and frac-stimulated gas-shales. First Break 32, 51–66. doi:10.3997/1365-2397.2014011

Barton, N., 1982. Modelling rock joint behaviour from in situ block tests: Implications for nuclear waste repository design. Columbus, OH.

Barton, N., Bandis, S., 1980. Some effects of scale on the shear strength of joints, in: International Journal of Rock Mechanics and Mining Sciences & Geomechanics Abstracts. Pergamon Press Ltd., pp. 69–73. doi:http://dx.doi.org/10.1016/0148-9062(80)90009-1

Barton, N., Bandis, S., Bakhtar, K., 1985. Strength, deformation and conductivity coupling of

472 rock joints. Int. J. Rock Mech. Min. Sci. Geomech. Abstr. 22, 121–140.
473 doi:10.1016/0148-9062(85)93227-9

474 Barton, N., Choubey, V., 1977. The shear strength of rock joints in theory and practice. Rock
475 Mech. Felsmechanik Mec. des Roches 10, 1–54. doi:10.1007/BF01261801

476 Belayneh, M.W., Matthäi, S.K., Blunt, M.J., Rogers, S.F., 2009. Comparison of deterministic
477 with stochastic fracture models in water-flooding numerical simulations. Am. Assoc.
478 Pet. Geol. Bull. 93, 1633–1648. doi:10.1306/07220909031

479 Bemis, S.P., Micklethwaite, S., Turner, D., James, M.R., Akciz, S., Thiele, S.T., Bangash,
480 H.A., 2014. Ground-based and UAV-Based photogrammetry: A multi-scale, high-
481 resolution mapping tool for structural geology and paleoseismology. J. Struct. Geol. 69,
482 163–178. doi:10.1016/j.jsg.2014.10.007

483 Bertotti, G., de Graaf, S., Bisdom, K., Vonhof, H.B., Reijmer, J.J.G., Bezerra, F.H.R.,
484 Cazarin, C., **accepted**. Fracturing and flow during post-rift subsidence in carbonate
485 rocks of the Jandaira Formation (NE Brazil). Basin Res.

486 Bisdom, K., Baud, E., Estrada, S., Sanz-Perl, Y., Gauthier, B., Bertotti, G., 2016a. Coupled
487 Stress-fluid Pressure Modelling of Stimulated Rock Volume in Shale - Impact of Natural
488 Fractures and Beef, in: 78th EAGE Conference & Exhibition. EAGE, Vienna, Austria.

489 Bisdom, K., Bertotti, G., Bezerra, F.H., **accepted**. Inter-well scale natural fracture geometry
490 and permeability variations in low-deformation carbonate rocks. J. Struct. Geol.

491 Bisdom, K., Bertotti, G., Nick, H.M., 2016b. The impact of in-situ stress and outcrop-based
492 fracture geometry on hydraulic aperture and upscaled permeability in fractured
493 reservoirs. Tectonophysics 690, 63–75. doi:10.1016/j.tecto.2016.04.006

494 Bisdom, K., Bertotti, G., Nick, H.M., 2016c. A geometrically based method for predicting

495 stress-induced fracture aperture and flow in discrete fracture networks. Am. Assoc. Pet.
496 Geol. Bull. 100, 1075–1097. doi:10.1306/02111615127

497 Bisdom, K., Bertotti, G., Nick, H.M., 2016d. The impact of different aperture distribution
498 models and critical stress criteria on equivalent permeability in fractured rocks. J.
499 Geophys. Res. Solid Earth 121, 4045–4063. doi:10.1002/2015JB012657

500 Bisdom, K., Gauthier, B.D.M., Bertotti, G., Hardebol, N.J., 2014. Calibrating discrete
501 fracture-network models with a carbonate three-dimensional outcrop fracture network:
502 Implications for naturally fractured reservoir modeling. Am. Assoc. Pet. Geol. Bull. 98,
503 1351–1376. doi:10.1306/02031413060

504 Bond, C.E., Shackleton, J.R., Wild, T., 2015. From Field Fractures to Reservoir Prediction:
505 Utilizing Drones, Virtual Outcrop and Digital Data Analysis to Input Into Discrete
506 Fracture Network (DFN) Models, in: AAPG Annual Convention and Exhibition.
507 Denver, Colorado.

508 Bonnet, E., Bour, O., Odling, N.E., Davy, P., Main, I., Cowie, P., Berkowitz, B., 2001.
509 Scaling of fracture systems in geological media. Rev. Geophys. 39, 347–383.
510 doi:10.1029/1999RG000074

511 Bour, O., Davy, P., 1997. Connectivity of random fault networks following a power law fault
512 length distribution. Water Resour. Res. 33, 1567–1583. doi:10.1029/96WR00433

513 Cottereau, N., Garcia, M.H., Gosselin, O.R., Vigier, L., 2010. Effective Fracture Network
514 Permeability: Comparative Study of Calculation Methods, in: SPE EUROPEC/EAGE
515 Annual Conference and Exhibition. Society of Petroleum Engineers, Barcelona, Spain.
516 doi:10.2118/131126-ms

517 Davy, P., Sornette, A., Sornette, D., 1990. Some consequences of a proposed fractal nature of

518 continental faulting. Nature 348, 56–58. doi:10.1038/348056a0

519 de Graaf, S., Reijmer, J.J.G., Bertotti, G. V., Bezerra, F.H.R., Cazarin, C.L., Bisdom, K.,
520 Vonhof, H.B., 2017. Fracturing and calcite cementation controlling fluid flow in the
521 shallow-water carbonates of the Jandaíra Formation, Brazil. Mar. Pet. Geol. 80, 382–
522 393. doi:10.1016/j.marpetgeo.2016.12.014

523 Dershowitz, W., 1985. Rock joint systems (Ph.D. Thesis). MIT. Massachusetts Institute of
524 Technology.

525 Dershowitz, W., Doe, T., 1997. Analysis of heterogeneously connected rock masses by
526 forward modeling of fractional dimension flow behavior. Int. J. Rock Mech. Min. Sci.
527 34, 61.e1-61.e19. doi:10.1016/S1365-1609(97)00237-2

528 Duelis Viana, C., Endlein, A., Ademar da Cruz Campanha, G., Henrique Grohmann, C.,
529 2016. Algorithms for extraction of structural attitudes from 3D outcrop models. Comput.
530 Geosci. 90, 112–122. doi:10.1016/j.cageo.2016.02.017

531 Durlofsky, L.J., 1991. Numerical calculation of equivalent grid block permeability tensors for
532 heterogeneous porous media. Water Resour. Res. 27, 699–708.
533 doi:10.1029/91WR00107

534 Egya, D., Geiger, S., Corbett, P., Bisdom, K., Bertotti, G., Bezerra, H., 2016. Assessing the
535 Validity and Limitations of Dual- porosity Models Using Geological Well Testing for
536 Fractured Formations, in: 78th EAGE Conference & Exhibition. EAGE, Vienna,
537 Austria.

538 Fabuel-Perez, I., Hodgetts, D., Redfern, J., 2010. Integration of digital outcrop models
539 (DOMs) and high resolution sedimentology – workflow and implications for geological
540 modelling: Oukaimeden Sandstone Formation, High Atlas (Morocco). Pet. Geosci. 16,

133–154. doi:10.1144/1354-079309-820

Geiger, S., Hehmeyer, O., Agada, S., Mutti, M., Benson, G., Shekhar, R., Toigulova, G., Chen, F., Christ, N., Amour, F., Agar, S., Immenhauser, A., 2013. Deciphering the Fundamental Controls of Flow in Carbonates Using Numerical Well-Testing, Production Optimisation, and 3D High-resolution Outcrop Analogues for Fractured Carbonate Reservoirs, in: Proceedings of 75th EAGE Conference & Exhibition Incorporating SPE EUROPEC 2013. Society of Petroleum Engineers. doi:10.2118/164805-MS

Geiger, S., Matthäi, S., 2012. What can we learn from high-resolution numerical simulations of single- and multi-phase fluid flow in fractured outcrop analogues? Geol. Soc. London, Spec. Publ. 374, 125–144. doi:10.1144/SP374.8

Hardebol, N.J., Bertotti, G., 2013. DigiFract: A software and data model implementation for flexible acquisition and processing of fracture data from outcrops. Comput. Geosci. 54, 326–336. doi:10.1016/j.cageo.2012.10.021

Hardebol, N.J., Maier, C., Nick, H., Geiger, S., Bertotti, G., Boro, H., 2015. Multiscale fracture network characterization and impact on flow: A case study on the Latemar carbonate platform. J. Geophys. Res. Solid Earth 120, 8197–8222. doi:10.1002/2015JB011879

Harwin, S., Lucieer, A., 2012. Assessing the accuracy of georeferenced point clouds produced via multi-view stereopsis from Unmanned Aerial Vehicle (UAV) imagery. Remote Sens. 4, 1573–1599. doi:10.3390/rs4061573

Hodgetts, D., 2013. Laser scanning and digital outcrop geology in the petroleum industry: A review. Mar. Pet. Geol. 46, 335–354. doi:10.1016/j.marpetgeo.2013.02.014

Hooker, J.N., Gale, J.F.W., Gomez, L.A., Laubach, S.E., Marrett, R., Reed, R.M., 2009.

564 Aperture-size scaling variations in a low-strain opening-mode fracture set, Cozzette
565 Sandstone, Colorado. J. Struct. Geol. 31, 707–718. doi:10.1016/j.jsg.2009.04.001

566 Hooker, J.N., Laubach, S.E., Marrett, R., 2014. A universal power-law scaling exponent for
567 fracture apertures in sandstones. Geol. Soc. Am. Bull. 126, 1340–1362.
568 doi:10.1130/B30945.1

569 James, M.R., Robson, S., 2012. Straightforward reconstruction of 3D surfaces and
570 topography with a camera: Accuracy and geoscience application. J. Geophys. Res. Earth
571 Surf. 117, 1–17. doi:10.1029/2011JF002289

572 Jonoud, S., Jackson, M.D., 2008. Validity of Steady-State Upscaling Techniques. SPE
573 Reserv. Eval. Eng. 11, 405–416. doi:10.2118/100293-PA

574 Karimi-Fard, M., Durlofsky, L.J., 2016. A general gridding, discretization, and coarsening
575 methodology for modeling flow in porous formations with discrete geological features.
576 Adv. Water Resour. m, 354–372. doi:10.1016/j.advwatres.2016.07.019

577 Lang, P.S., Paluszny, A., Zimmerman, R.W., 2014. Permeability tensor of three-dimensional
578 fractured porous rock and a comparison to trace map predictions. J. Geophys. Res. Solid
579 Earth 119, 6288–6307. doi:10.1002/2014JB011027

580 Lawn, B.R., Wilshaw, T.R., 1975. Fracture of brittle solids. Cambridge University Press.

581 Lei, Q., Latham, J., Xiang, J., Tsang, C.-F., 2015. Polyaxial stress-induced variable aperture
582 model for persistent 3D fracture networks. Geomech. Energy Environ. 1, 34–47.
583 doi:10.1016/j.gete.2015.03.003

584 Lei, Q., Latham, J.-P., Xiang, J., Tsang, C.-F., Lang, P., Guo, L., 2014. Effects of
585 geomechanical changes on the validity of a discrete fracture network representation of a
586 realistic two-dimensional fractured rock. Int. J. Rock Mech. Min. Sci. 70, 507–523.

587 doi:10.1016/j.ijrmms.2014.06.001

588 Lei, Q., Wang, X., Xiang, J., Latham, J.-P., 2016. Influence of stress on the permeability of a
589 three-dimensional fractured sedimentary layer. 50th US Rock Mech. / Geomech. Symp.
590 586.

591 Lin, Y., Jiang, M., Yao, Y., Zhang, L., Lin, J., 2015. Use of UAV oblique imaging for
592 detection of individual trees in residential environments. Urban For. Urban Green. 14,
593 404–412. doi:10.1016/j.ufug.2015.03.003

594 Long, J.C.S., Witherspoon, P.A., 1985. The relationship of the degree of interconnection to
595 permeability in fracture networks. J. Geophys. Res. 90, 3087.
596 doi:10.1029/JB090iB04p03087

597 Mahmud, K., Mariethoz, G., Treble, P.C., Baker, A., 2015. Terrestrial LiDAR Survey and
598 Morphological Analysis to Identify Infiltration Properties in the Tamala Limestone,
599 Western Australia. IEEE J. Sel. Top. Appl. Earth Obs. Remote Sens. 8, 4871–4881.
600 doi:10.1109/JSTARS.2015.2451088

601 Makedonska, N., Hyman, J.D., Karra, S., Painter, S.L., Gable, C.W., Viswanathan, H.S.,
602 2016. Evaluating the effect of internal aperture variability on transport in kilometer scale
603 discrete fracture networks. Adv. Water Resour. 94, 486–497.
604 doi:10.1016/j.advwatres.2016.06.010

605 Martinez-Landa, L., Carrera, J., Pérez-Estaún, A., Gomez, P., Bajos, C., 2016. Structural
606 geology and geophysics as a support to build a hydrogeologic model of granite rock.
607 Solid Earth 7, 881–895. doi:10.5194/se-7-881-2016

608 Matthäi, S.K., Belayneh, M., 2004. Fluid flow partitioning between fractures and a permeable
609 rock matrix. Geophys. Res. Lett. 31. doi:10.1029/2003GL019027

610 Matthäi, S.K., Geiger, S., Roberts, S.G., Paluszny, A., Belayneh, M., Burri, A., Mezentsev,
611 A., Lu, H., Coumou, D., Driesner, T., Heinrich, C.A., 2007. Numerical simulation of
612 multi-phase fluid flow in structurally complex reservoirs. Geol. Soc. London, Spec.
613 Publ. 292, 405–429. doi:10.1144/SP292.22

614 Mauldon, M., 1998. Estimating Mean Fracture Trace Length and Density from Observations
615 in Convex Windows. Rock Mech. Rock Eng. 31, 201–216. doi:10.1007/s006030050021

616 Mauldon, M., Dunne, W.M., Rohrbaugh, M.B., 2001. Circular scanlines and circular
617 windows: New tools for characterizing the geometry of fracture traces. J. Struct. Geol.
618 23, 247–258. doi:10.1016/S0191-8141(00)00094-8

619 Muhammad, F., 2016. Geological well testing in fractured carbonate reservoir. Heriot Watt
620 University.

621 Nejati, M., Paluszny, A., Zimmerman, R.W., 2016. A finite element framework for modeling
622 internal frictional contact in three-dimensional fractured media using unstructured
623 tetrahedral meshes. Comput. Methods Appl. Mech. Eng. 306, 123–150.
624 doi:10.1016/j.cma.2016.03.028

625 Nelson, R.A., 2001. Geologic Analysis of Naturally Fractured Reservoirs, in: Geologic
626 Analysis of Naturally Fractured Reservoirs. Gulf Professional Publishing, Woburn, MA,
627 USA, pp. 101–124.

628 Nick, H.M., Matthäi, S.K., 2011a. A Hybrid Finite-Element Finite-Volume Method with
629 Embedded Discontinuities for Solute Transport in Heterogeneous Media. Vadose Zo. J.
630 10, 299. doi:10.2136/vzj2010.0015

631 Nick, H.M., Matthäi, S.K., 2011b. Comparison of Three FE-FV Numerical Schemes for
632 Single- and Two-Phase Flow Simulation of Fractured Porous Media. Transp. Porous

633 Media 90, 421–444. doi:10.1007/s11242-011-9793-y

634 Nick, H.M., Paluszny, A., Blunt, M.J., Matthai, S.K., 2011. Role of geomechanically grown
635 fractures on dispersive transport in heterogeneous geological formations. Phys. Rev. E
636 84, 56301. doi:10.1103/PhysRevE.84.056301

637 Oda, M., 1985. Permeability tensor for discontinuous rock masses. Géotechnique 35, 483–
638 495.

639 Olson, J.E., 2003. Sublinear scaling of fracture aperture versus length: An exception or the
640 rule? J. Geophys. Res. Solid Earth 108, 2413. doi:10.1029/2001JB000419

641 Olson, J.E., Laubach, S.E., Lander, R.H., 2009. Natural fracture characterization in tight gas
642 sandstones: Integrating mechanics and diagenesis. Am. Assoc. Pet. Geol. Bull. 93,
643 1535–1549. doi:10.1306/08110909100

644 Olson, J.E., Schultz, R.A., 2011. Comment on "A note on the scaling relations for opening
645 mode fractures in rock" by C.H. Scholz. J. Struct. Geol. 33, 1523–1524.
646 doi:10.1016/j.jsg.2011.07.004

647 Olsson, R., Barton, N., 2001. An improved model for hydromechanical coupling during
648 shearing of rock joints. Int. J. Rock Mech. Min. Sci. 38, 317–329. doi:10.1016/S1365-
649 1609(00)00079-4

650 Ortega, O.J., Marrett, R.A., Laubach, S.E., 2006. A scale-independent approach to fracture
651 intensity and average spacing measurement. Am. Assoc. Pet. Geol. Bull. 90, 193–208.
652 doi:10.1306/08250505059

653 Pahl, P.J., 1981. Estimating the mean length of discontinuity traces. Int. J. Rock Mech. Min.
654 Sci. Geomech. Abstr. 18, 221–228. doi:10.1016/0148-9062(81)90976-1

655 Paluszny, A., Matthäi, S.K., Hohmeyer, M., 2007. Hybrid finite element-finite volume

656 discretization of complex geologic structures and a new simulation workflow
657 demonstrated on fractured rocks. Geofluids 7, 186–208. doi:10.1111/j.1468-
658 8123.2007.00180.x

659 Philip, Z.G., Jennings, J.W., Olson, J.E., Laubach, S.E., Holder, J., 2005. Modeling Coupled
660 Fracture-Matrix Fluid Flow in Geomechanically Simulated Fracture Networks. SPE
661 Reserv. Eval. Eng. 8, 300–309. doi:10.2118/77340-PA

662 Pollard, D.D., Segall, P., 1987. Theoretical displacements and stresses near fractures in rock:
663 with applications to faults, veins, dikes, and solution surfaces, in: Fracture Mechanics of
664 Rock. Elsevier, pp. 277–349. doi:10.1016/B978-0-12-066266-1.50013-2

665 Reif, D., Grasemann, B., Faber, R.H., 2011. Quantitative structural analysis using remote
666 sensing data: Kurdistan, northeast Iraq. Am. Assoc. Pet. Geol. Bull. 95, 941–956.
667 doi:10.1306/11151010112

668 Reith, D.F.H., 2015. Analysis of the different impacts influencing the value of the fractal
669 dimension regarding the Whitby Mudstone formation (UK) & Jandaira formation
670 (Brazil). Delft University of Technology.

671 Rotevatn, A., Buckley, S.J., Howell, J.A., Fossen, H., 2009. Overlapping faults and their
672 effect on fluid flow in different reservoir types: A LIDAR-based outcrop modeling and
673 flow simulation study. Am. Assoc. Pet. Geol. Bull. 93, 407–427.
674 doi:10.1306/09300807092

675 Sanderson, D.J., Nixon, C.W., 2015. The use of topology in fracture network
676 characterization. J. Struct. Geol. 72, 55–66. doi:10.1016/j.jsg.2015.01.005

677 Scholz, C.H., 2011. Reply to comments of Jon Olson and Richard Schultz. J. Struct. Geol. 33,
678 1525–1526. doi:10.1016/j.jsg.2011.07.006

679 Shah, S., Møyner, O., Tene, M., Lie, K.A., Hajibeygi, H., 2016. The multiscale restriction
680 smoothed basis method for fractured porous media (F-MsRSB). J. Comput. Phys. 318,
681 36–57. doi:10.1016/j.jcp.2016.05.001

682 Tao, Q., Ehlig-Economides, C.A., Ghassemi, A., 2009. Investigation of Stress-Dependent
683 Permeability in Naturally Fractured Reservoirs Using a Fully Coupled Poroelastic
684 Displacement Discontinuity Model, in: SPE Annual Technical Conference and
685 Exhibition. Society of Petroleum Engineers, New Orleans, Louisiana.
686 doi:10.2118/124745-MS

687 Tavani, S., Corradetti, A., Billi, A., 2016. High precision analysis of an embryonic
688 extensional fault-related fold using 3D orthorectified virtual outcrops: The viewpoint
689 importance in structural geology. J. Struct. Geol. 86, 200–210.
690 doi:10.1016/j.jsg.2016.03.009

691 Tavani, S., Granado, P., Corradetti, A., Girundo, M., Iannace, A., Arbués, P., Muñoz, J. a.,
692 Mazzoli, S., 2014. Building a virtual outcrop, extracting geological information from it,
693 and sharing the results in Google Earth via OpenPlot and Photoscan: An example from
694 the Khaviz Anticline (Iran). Comput. Geosci. 63, 44–53.
695 doi:10.1016/j.cageo.2013.10.013

696 Ullman, S., 1979. The Interpretation of Structure from Motion. Proc. R. Soc. B Biol. Sci. 203,
697 405–426. doi:10.1098/rspb.1979.0006

698 Vasuki, Y., Holden, E.-J., Kovesi, P., Micklethwaite, S., 2014. Semi-automatic mapping of
699 geological Structures using UAV-based photogrammetric data: An image analysis
700 approach. Comput. Geosci. 69, 22–32. doi:10.1016/j.cageo.2014.04.012

701 Vermilye, J.M., Scholz, C.H., 1995. Relation between vein length and aperture. J. Struct.
702 Geol. 17, 423–434. doi:10.1016/0191-8141(94)00058-8

703 Vollgger, S.A., Cruden, A.R., 2016. Mapping folds and fractures in basement and cover rocks
704 using UAV photogrammetry, Cape Liptrap and Cape Paterson, Victoria, Australia. J.
705 Struct. Geol. 85, 168–187. doi:10.1016/j.jsg.2016.02.012

706 Wilson, C.E., Aydin, A., Karimi-Fard, M., Durlofsky, L.J., Amir, S., Brodsky, E.E., Kreylos,
707 O., Kellogg, L.H., 2011. From outcrop to flow simulation: Constructing discrete fracture
708 models from a LIDAR survey. Am. Assoc. Pet. Geol. Bull. 95, 1883–1905.
709 doi:10.1306/03241108148

710 Wu, H.Q., Pollard, D.D., 2002. Imaging 3-D fracture networks around boreholes. Am. Assoc.
711 Pet. Geol. Bull. 86, 593–604. doi:10.1306/61EEDB52-173E-11D7-8645000102C1865D

712 Zhang, L., Einstein, H.H., 1998. Estimating the Mean Trace Length of Rock Discontinuities.
713 Rock Mech. Rock Eng. 31, 217–235. doi:10.1007/s006030050022

714 Zoback, M.D., 2007. Reservoir Geomechanics, Reservoir Geomechanics. Cambridge
715 University Press, Cambridge. doi:10.1017/CBO9780511586477

716

717

# Appendix A – Summary of aperture methods

## *(Sub-)linear length-aperture scaling*

Linear Elastic Fracture Mechanics (LEFM) predicts that aperture scales (sub-)linearly with length during propagation of fractures (Atkinson, 1984; Olson, 2003; Pollard and Segall, 1987). Maximum opening at the centre of the fracture, $d_{max}$, is defined by fracture toughness $K_C$, the Poisson's ratio $\nu$, Young's modulus E and fracture length L:

$$d_{\max} = \frac{K_C\left(1-\nu^2\right)}{E\sqrt{\frac{\pi}{8}}}\sqrt{L},$$

where $K_C$ is a function of driving stress $\Delta\sigma_I$ and fracture length:

$$K_C = \Delta\sigma_I\sqrt{\pi L/2}.$$

Discussion remains on whether aperture scales linear or sublinear with length, which has large implications for apertures of relatively large fractures (Olson, 2003; Olson and Schultz, 2011; Scholz, 2011; Vermilye and Scholz, 1995). The impact of linear versus sublinear scaling on permeability is investigated in (Bisdom et al., 2016d).

## *Power-law scaling*

Outcrop studies typically find that fracture lengths follow power-law scaling distributions (e.g. Bonnet et al., 2001; Bour and Davy, 1997). This, combined with the linear length-aperture scaling model, implies that aperture also follows power-law scaling relations. Power-law scaling of apertures is commonly observed in outcrops (Hooker et al., 2014, 2009; Ortega et al., 2006), although the relation with length is rarely studied in outcrops. Instead, the aperture distributions are defined independent of other geometrical or geomechanical parameters, through a power-law function:

739 $$F = aX^{-b},$$

740 where $F$ is the cumulative frequency, $a$ is a density constant and $b$ is the power-law scaling
741 exponent (Bonnet et al., 2001). Power-law aperture distributions are the preferred method of
742 defining aperture in industry fractured reservoir models, but they are rarely related to any
743 other geometrical parameter. As a result, short fractures may be assigned unrealistically large
744 apertures (Bisdom et al., 2016d).

745 *Barton-Bandis*

746 Whereas (sub-)linear length-aperture scaling predicts opening during propagation over
747 geological times, Barton-Bandis describes present-day opening in the current stress field,
748 assuming that fractures have irregular walls that result in conductive fractures when shearing
749 occurs, even when fluid pressures are low (Bandis, 1980; Bandis et al., 1983; Barton, 1982;
750 Barton and Bandis, 1980; Barton and Choubey, 1977). Mechanical aperture $E_n$ is a function
751 of an intrinsic initial aperture $E_0$, maximum closure $v_m$, toughness $K_{ni}$ and driving stress $\Delta\sigma_I$
752 (e.g. Barton, 2014).

753 $$E_n = E_0 - \left( \frac{1}{v_m} + \frac{K_{ni}}{\Delta\sigma_I} \right)^{-1}.$$

754 Hydraulic aperture $e$ is a function of mechanical aperture, the Joint Roughness Coefficient
755 (JRC) and the ratio between shear ($u_{geom}$) and peak shear ($u_{peak}$) displacement (Olsson and
756 Barton, 2001).

757 $$e = \begin{cases} \dfrac{E_n^{\,2}}{JRC^{2.5}} & for \dfrac{u_{geom}}{u_{peak}} \le 0.75 \\ \sqrt{E_n}\, JRC_{mob} & for \dfrac{u_{geom}}{u_{peak}} \ge 1 \end{cases}.$$

This aperture model is strongly dependent on the local normal and shear stress acting on each fracture segment, which is most accurately determined using geomechanical Finite-Element models with discrete fractures (Bisdom et al., 2016b; Lei et al., 2014).

Alternatively, an approximation of Barton-Bandis apertures can be made without use of numerical models. Using a far field stress and fracture geometry, aperture can be approximated (Bisdom et al., 2016c). This model is strongly dependent on stress angle α between fracture strike and $\sigma_1$:

$$\sigma_{n,\text{angle}} = 0.0054\sigma_1\alpha + 1.5186\sigma_1^{0.723}.$$

Normal stress is further corrected for length L and spacing S:

$$\sigma_{n,geom} = \sigma_{n,\text{angle}}(-0.083\ln L + 1.055)\cdot 0.996\cdot S^{-0.008}.$$

Shear displacement is also defined as a function of length and stress angle:

$$u_{geom} = L\cdot\sigma_1\cdot\alpha\left(-9.07\cdot10^{-8}\alpha + 8.1\cdot10^{-6}\right).$$

# Figures

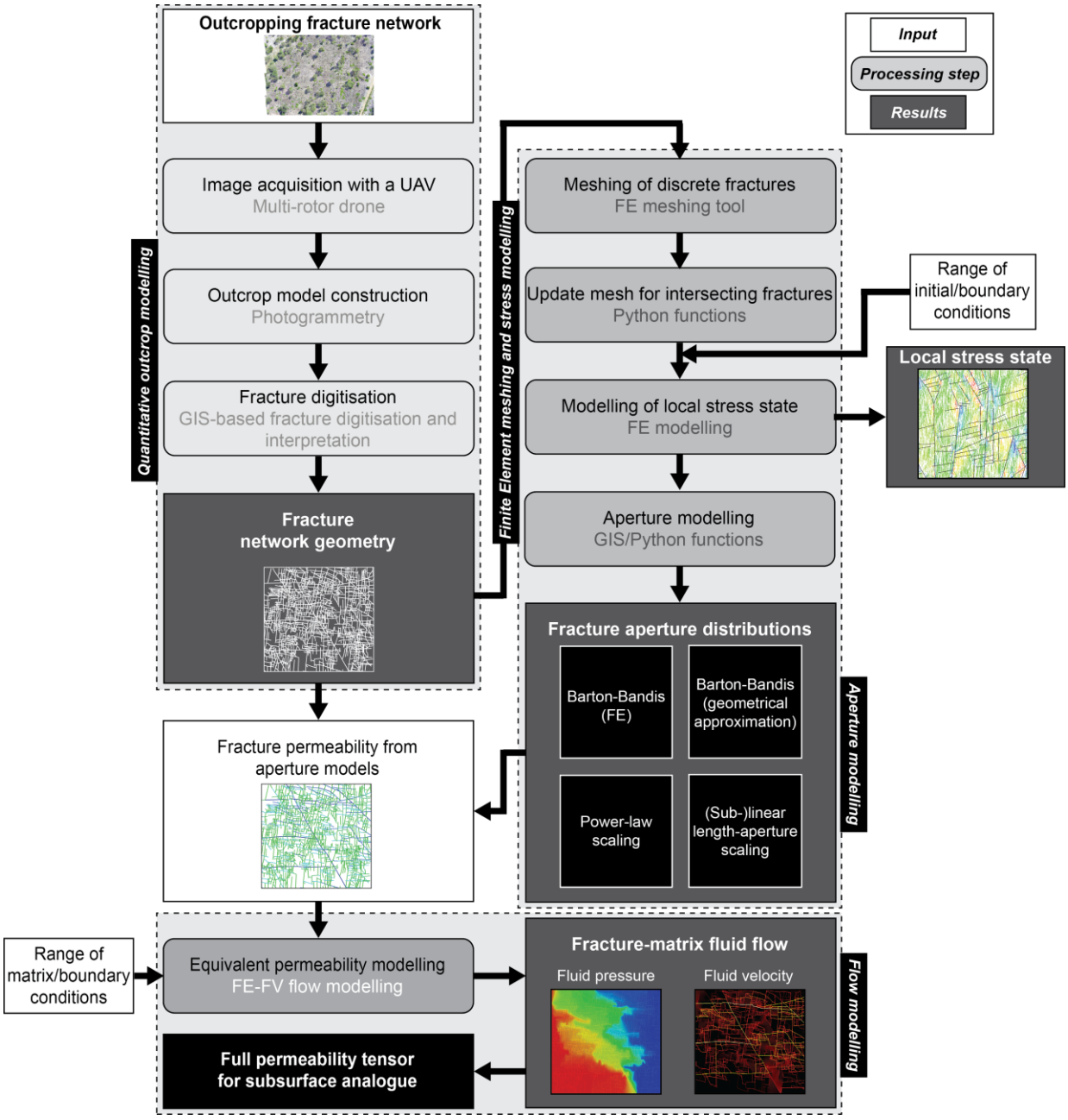


*Figure 1 Workflow for obtaining flow-based principal permeability from outcropping fracture networks that are representative of subsurface reservoir stress and pressure conditions, by taking into account the impact of stress on aperture and flow. See Appendix A for details on the aperture models.*

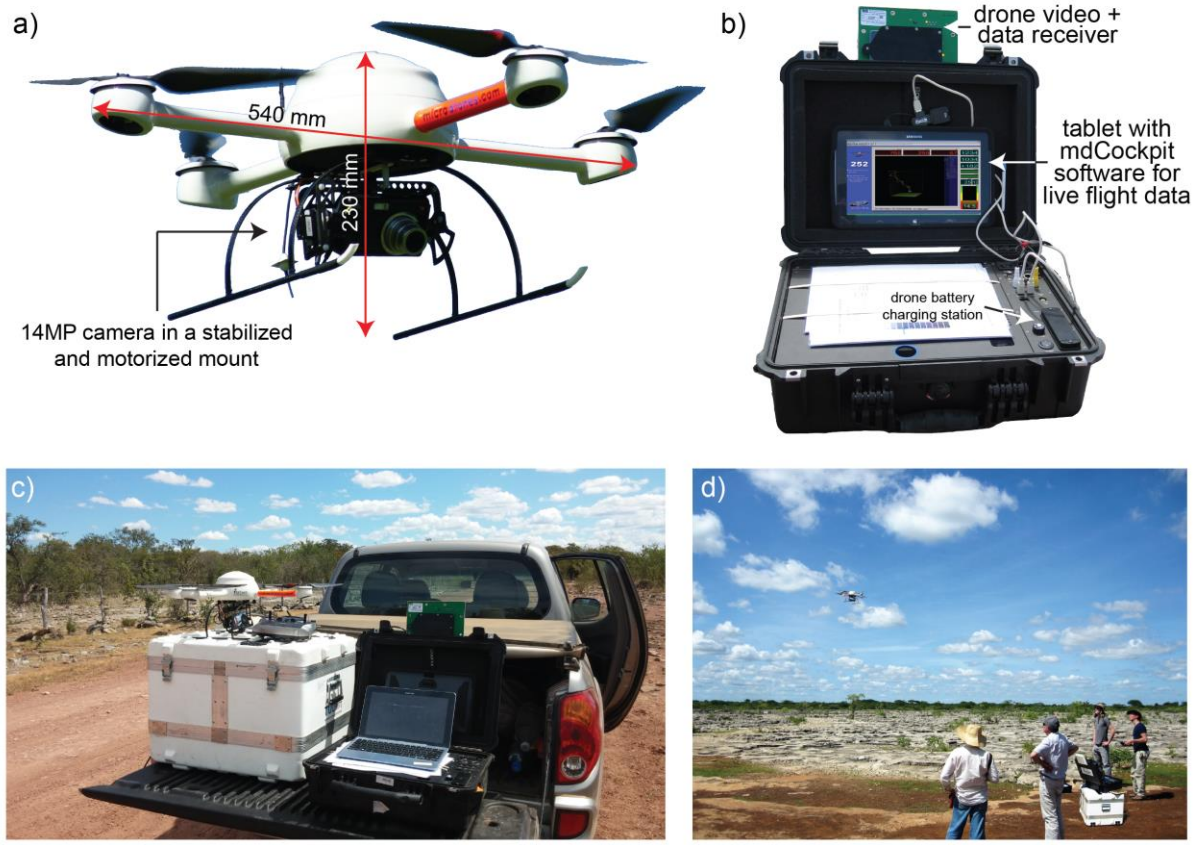


776

777 *Figure 2 Overview of the UAV equipment in the field: a) UAV (microdrones md4-200) with*

778 *compact camera; b) Base station with receivers and tablet to receive and store flight data*

779 *and video; c) Preparation for UAV deployment in the field. White case is the UAV transport*

780 *case; d) Use of the UAV to image carbonate pavements.*

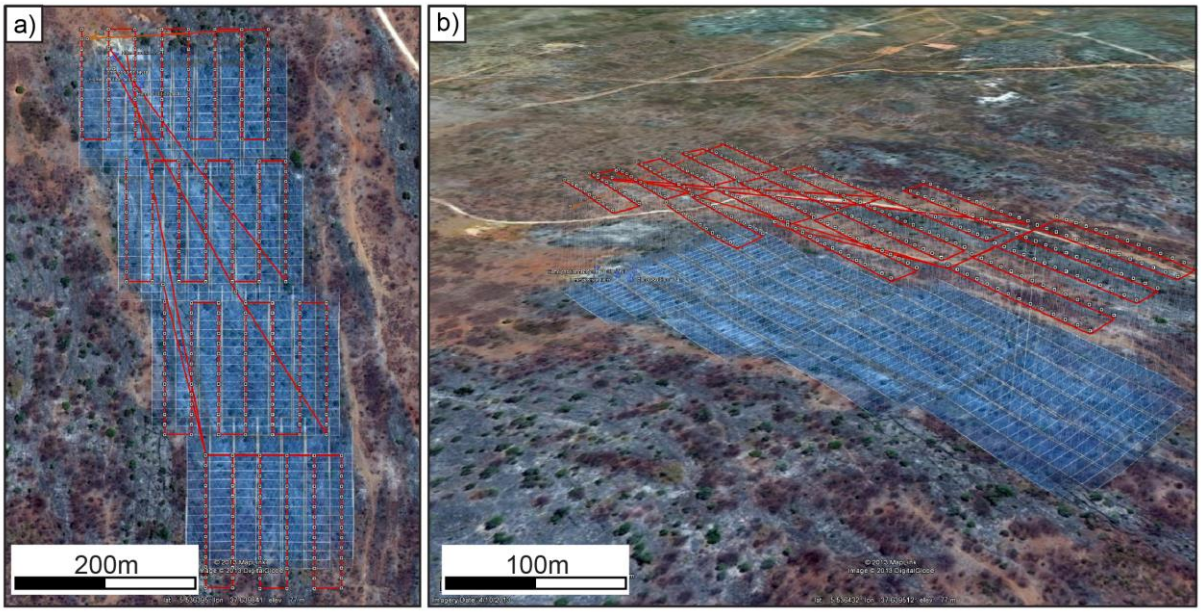


781

782 *Figure 3 Programming and visualising GNSS-steered flights: a) Top view of flight path (red)*
783 *and imaged area (blue) in Google Earth; b) 3-D of the flight path, allowing for checking the*
784 *programmed flight altitude with respect to ground level.*

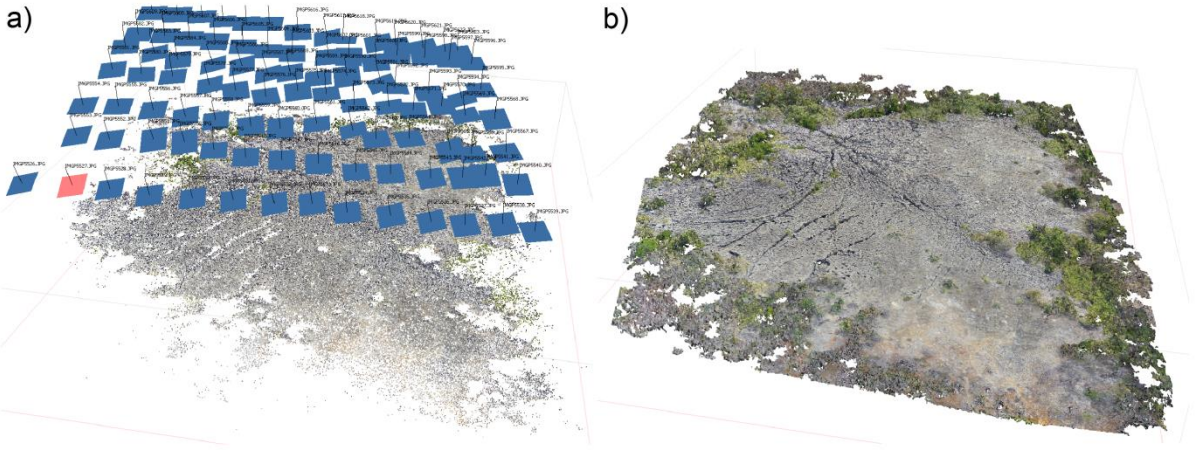


785

786 *Figure 4 Generating a 3-D outcrop model from georeferenced photographs using*
787 *photogrammetry: a) Alignment of the images (rectangles) based on their GNSS position and*
788 *common points extracted from the images. The image name is shown for each image (small*
789 *texts); b) 3-D high-resolution point cloud of the outcrop.*

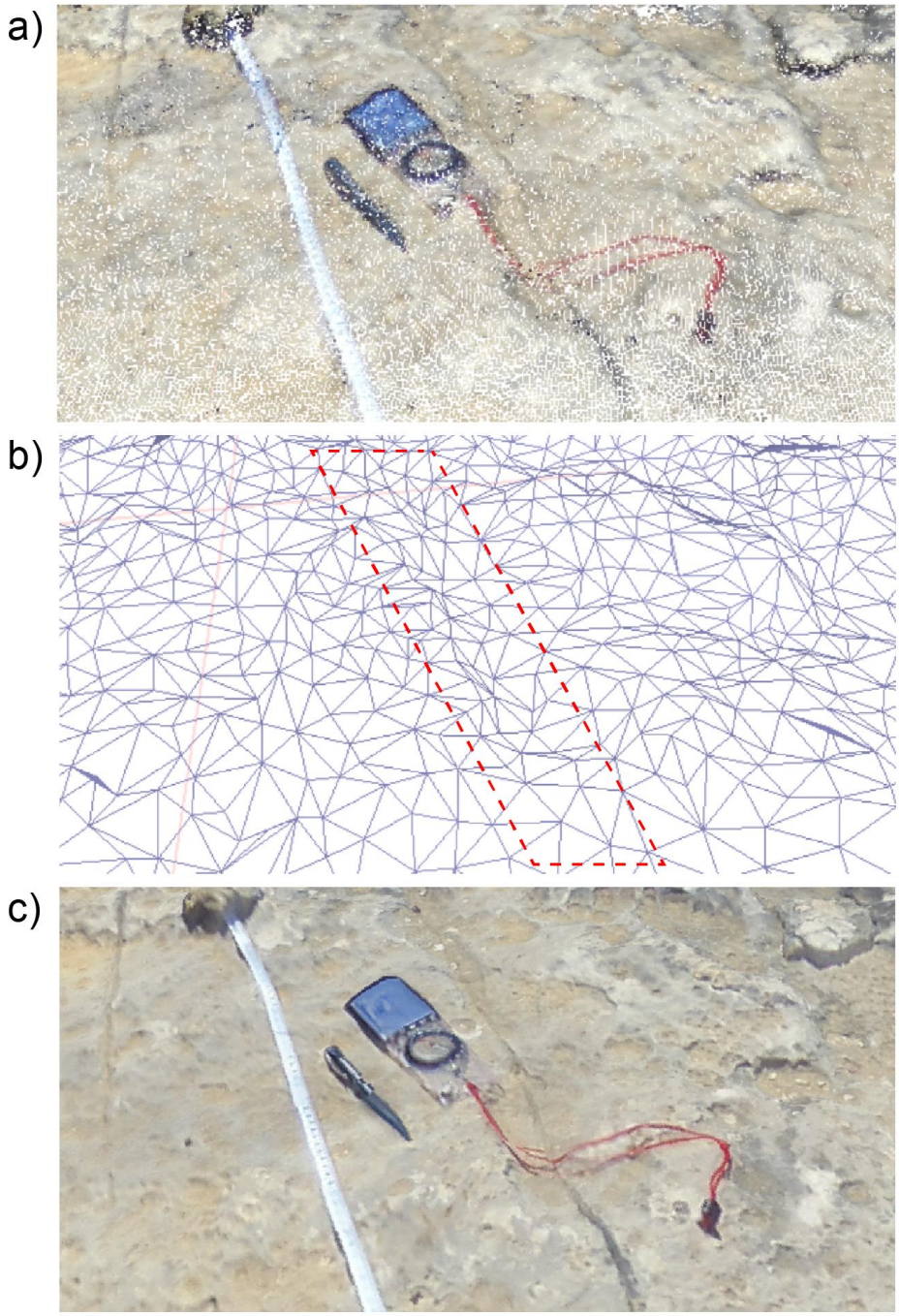


*Figure 5 Constructing a 3-D meshed surface from the point cloud: a) Detail view of the dense point cloud with a resolution of 1.4x10$^4$ points per m$^2$, showing a compass and pen for scale; b) Triangular mesh constructed for the area from (a). The mesh has a lower resolution than the point cloud, but does still indicate the main discontinuities, such as the fracture within the red dashed area; c) Texture extracted from the original photographs, projected onto the mesh.*

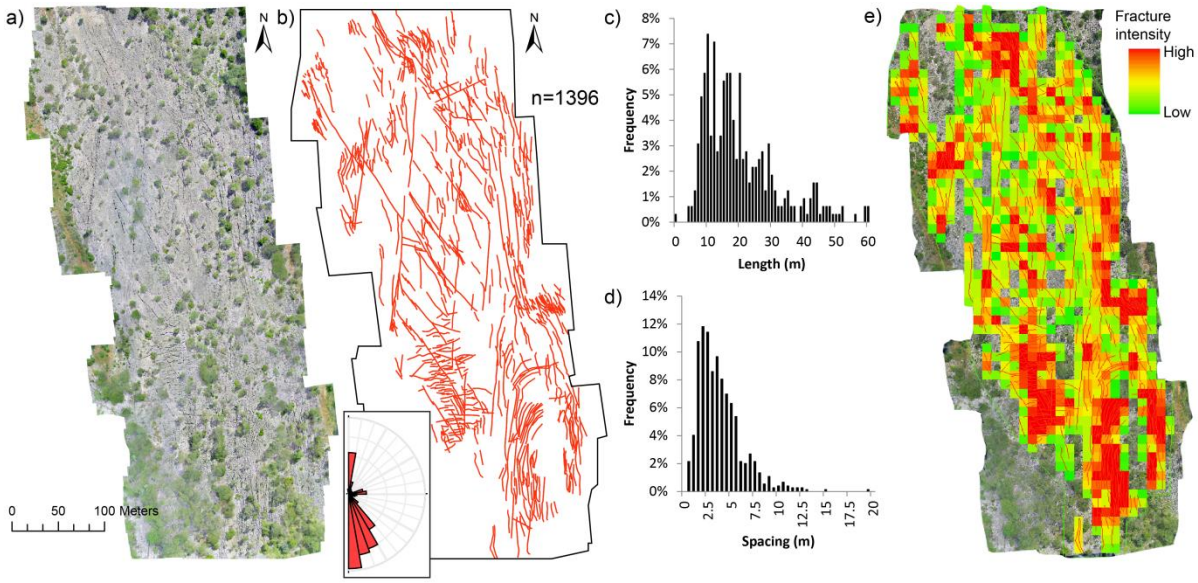


797

798 *Figure 6 Fracture digitisation and analysis in DigiFract using a 2-D orthomosaic of a*
799 *carbonate pavement, constructed from 400 photographs taken from an altitude of 50 m,*
800 *resulting in a orthomosaic resolution of 1.44 cm/px: a) The orthomosaic used for fracture*
801 *digitisation; b) The digitised fracture network; c) Fracture length distribution; d) Fracture*
802 *spacing distribution calculated using a box-counting method; e) Spatial fracture intensity*
803 *calculated using box-counting.*

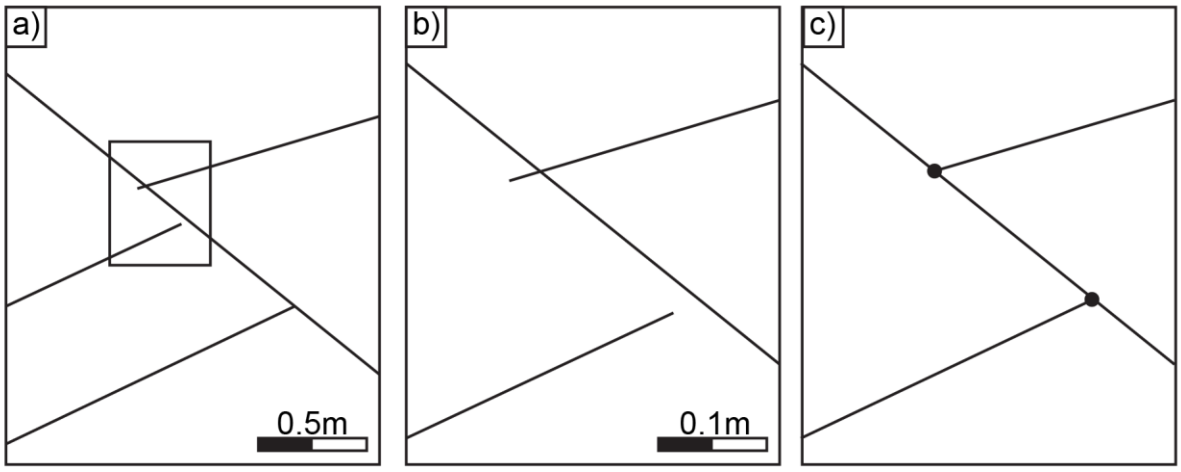


804

805 *Figure 7 Removal of minor gaps and overlaps to accurately represent the network topology:*
806 *a) Three small fractures terminating against one larger fracture, with incorrect connections;*

*b) Detail showing one overlapping segment and one segment with a gap; c) Correct fracture network interpretation using snapping.*

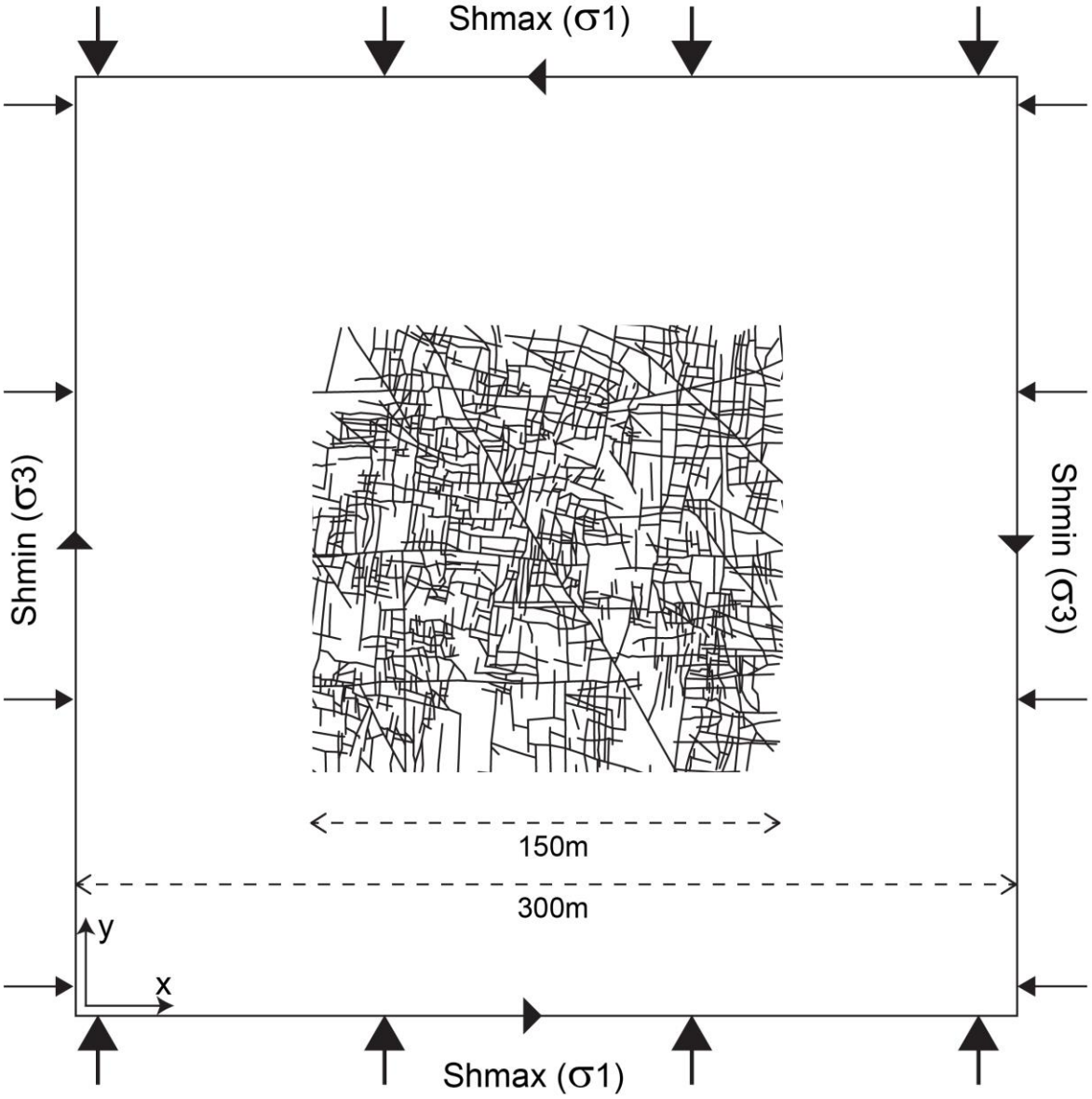


*Figure 8 Set-up of an elastic mechanical fracture network, using a 50 m × 50 m fracture pattern from a carbonate outcrop in central Tunisia* (Bisdom et al., 2016b). *Maximum horizontal stress $\sigma_1$ (30 MPa) is applied in the y-direction, resulting in a $\sigma_3$ of 10 MPa in the x-direction, for a Poisson's ratio of 0.3. We apply displacement boundary conditions on the centre points of each boundary to ensure symmetrical deformation.*

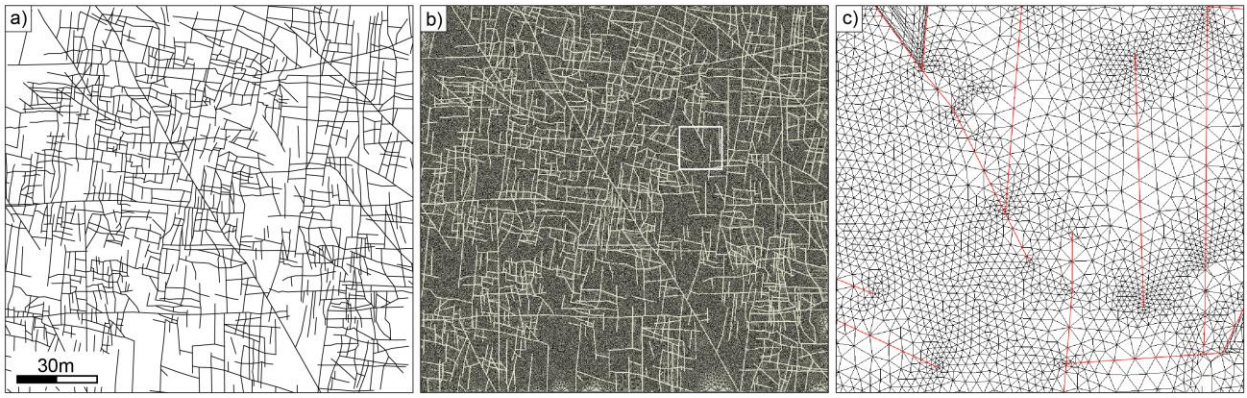


*Figure 9 Converting a deterministic fracture network into a triangular mesh: a) 150 m × 142 m section extracted from an outcropping carbonate pavement in the Potiguar basin (NE Brazil); b) Meshed fracture network geometry; c) detail of the mesh showing refinement around the fracture terminations and intersections (location indicated by the white square in (b).*

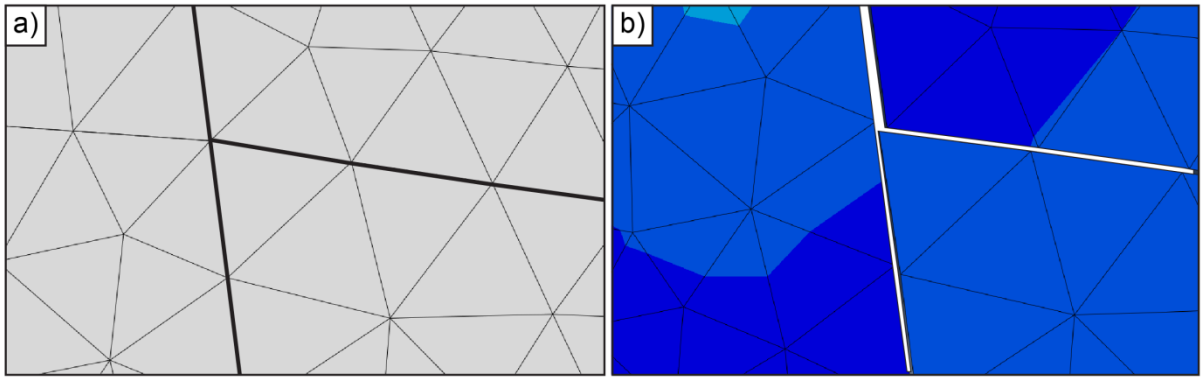


*Figure 10 Aperture in the FE models is modelled by representing the fractures as seams in the mesh, which can open or close as a function of local stress: a) Input mesh with two fractures indicated by the thick lines; b) Result after simulation, showing the stresses in the mesh and the resulting fracture opening along the seams.*

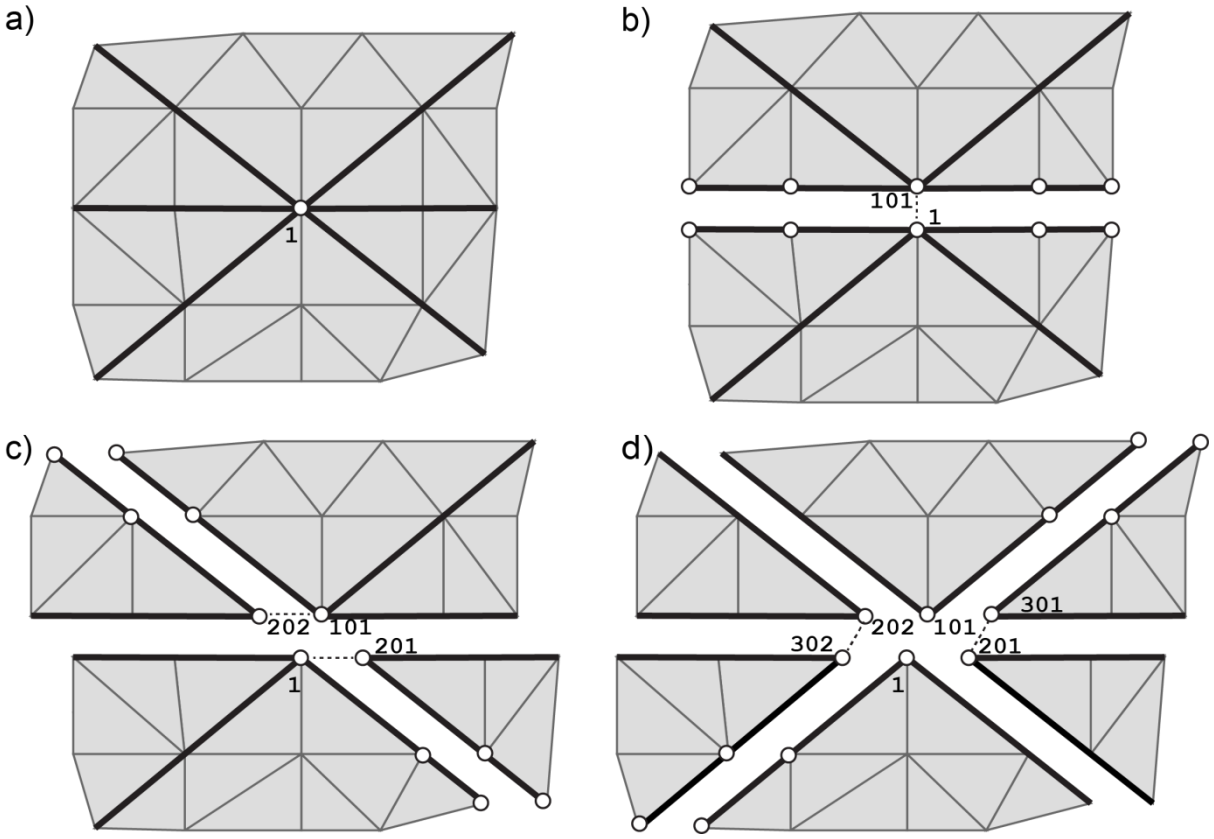


*Figure 11 Example illustrating the process of generating complex fracture intersections for three fractures that share a single intersection. The original node at this intersection, with identifier 1, is duplicated several times to generate the intersecting seams: a) Original mesh with fractures indicated by bold lines; b) Generating the first fracture by splitting nodes – node 1 is duplicated to 101; c) Second fracture requires duplication of both node 1 and 101 (1→201, 101→202); d) The third intersecting fracture requires duplication of the last two nodes formed (201→301, 202→302).*

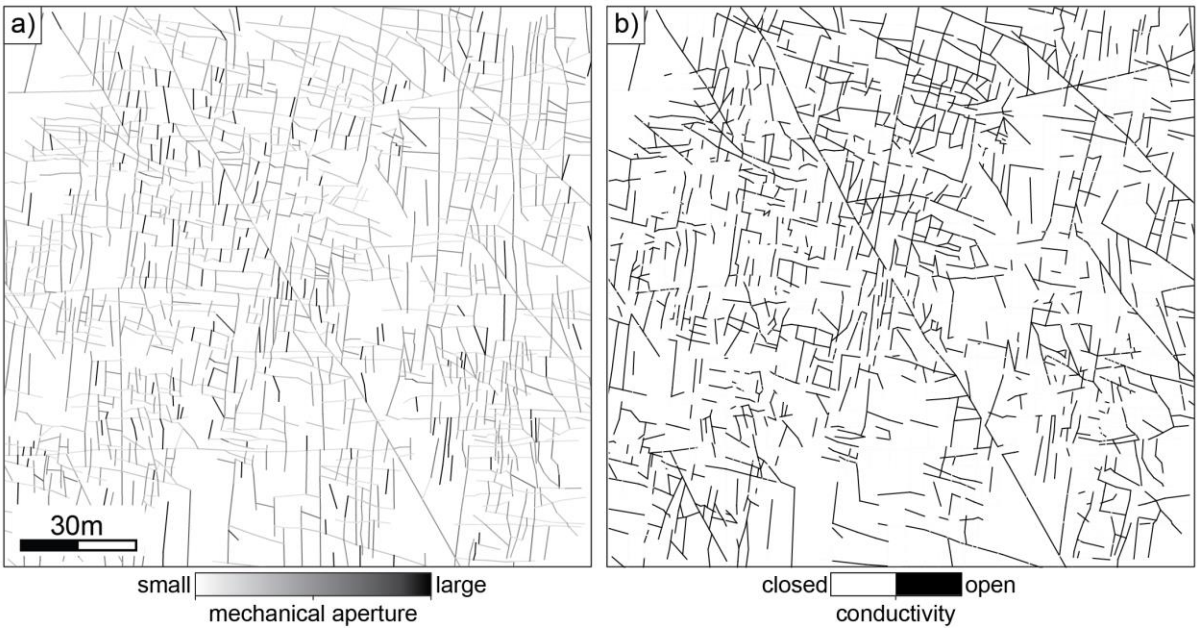


834

835 *Figure 12 Stress-induced aperture modelling: a) Mechanical aperture defined by Barton-*
836 *Bandis, calculated from normal and shear stresses acting on each fracture segment, under a*
837 *N-S regional $\sigma_1$ of 30 MPa and an E-W $\sigma_3$ of 10 MPa; b) Identification of hydraulically*
838 *conductive fractures using the Barton-Bandis model, for the same stress boundary*
839 *conditions.*

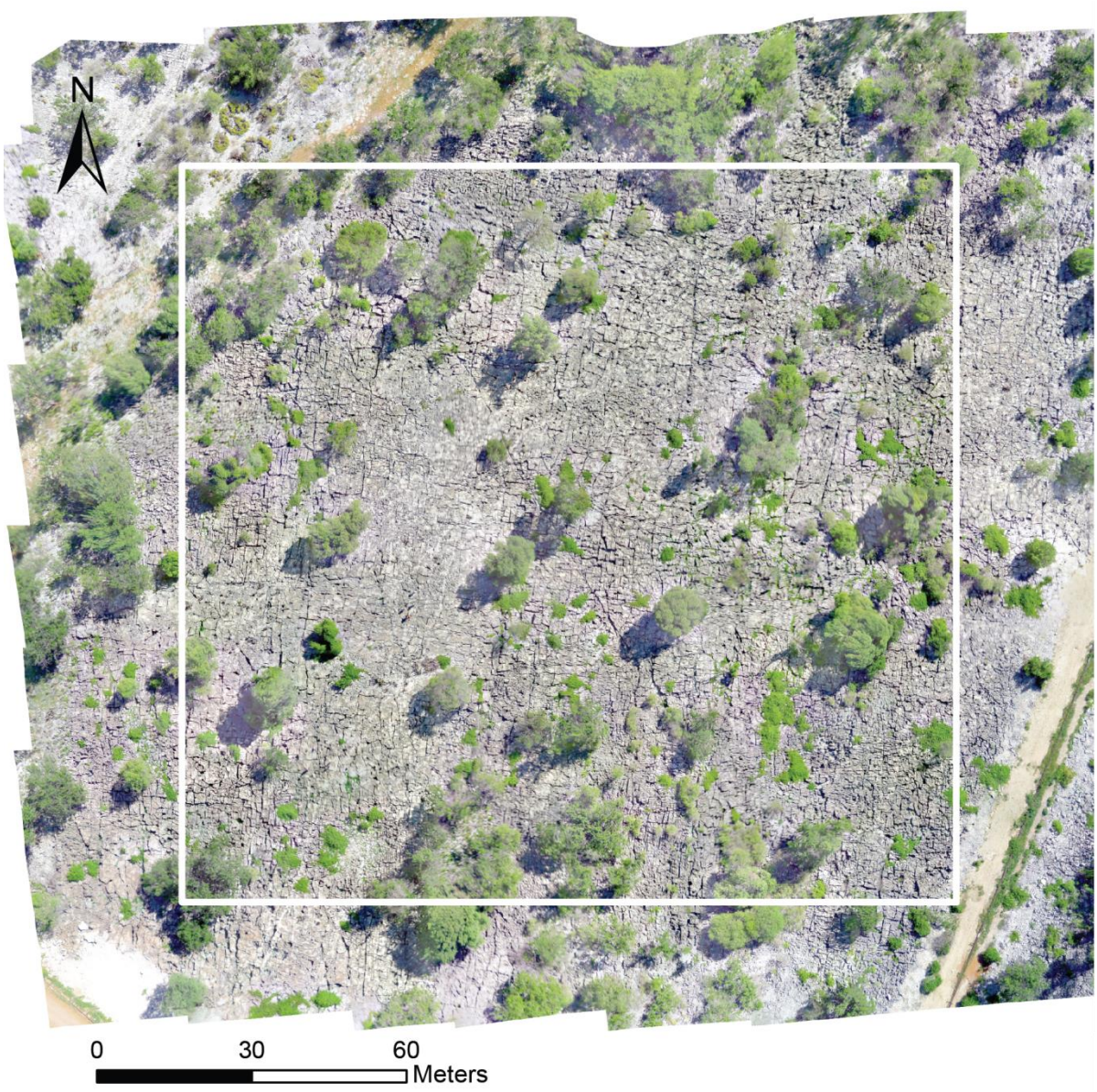


840

841 *Figure 13 High-resolution orthomosaic (1.44 cm/px resolution) of part of an outcrop in the*

842 *Potiguar basin (lat/long: -5.53092°, -37.6283°) constructed from 90 georeferenced images.*

843 *The white boundary indicates the domain that is considered for stress and flow modelling.*

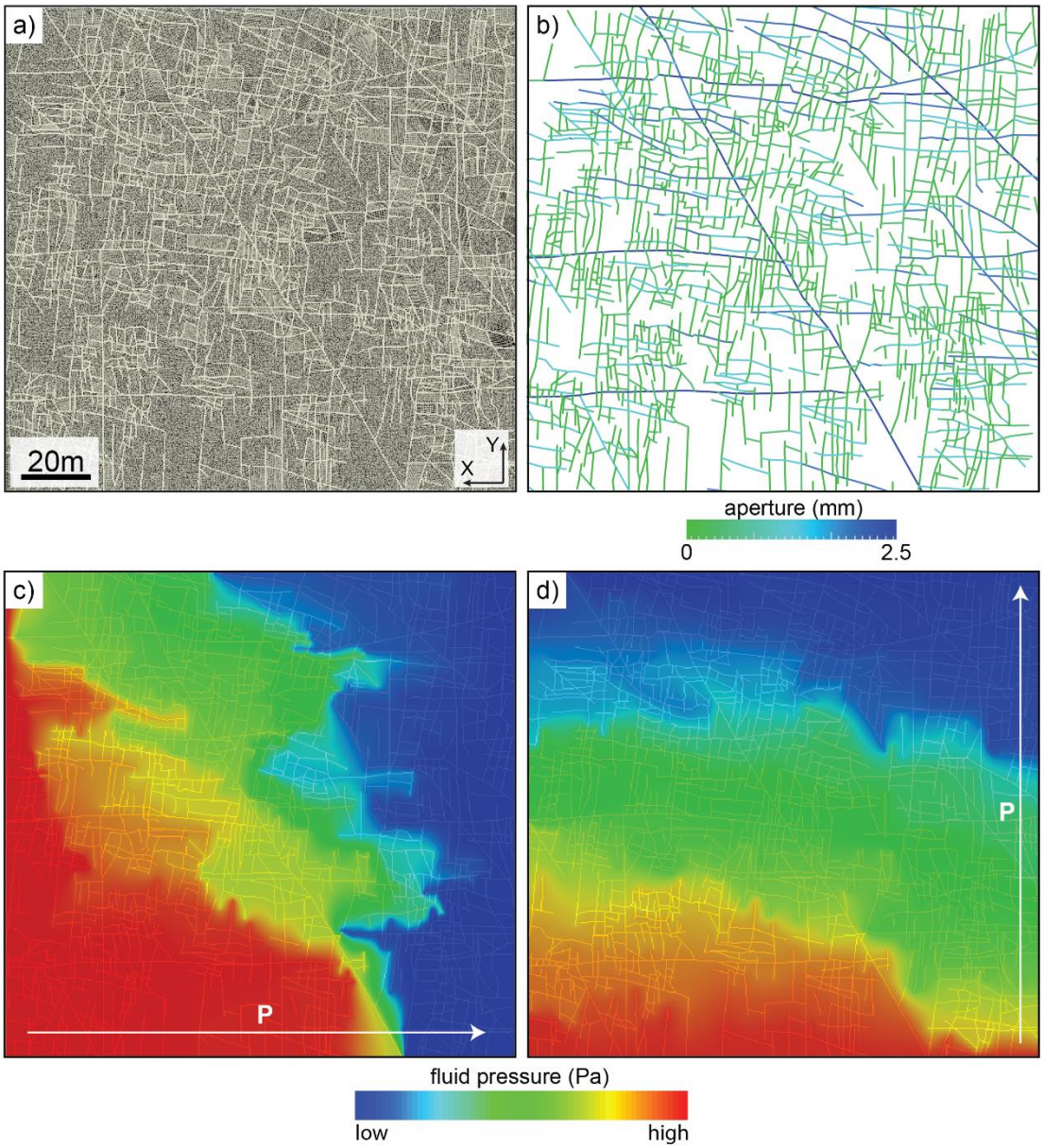


844

845 *Figure 14 Aperture and permeability results: a) 2-D mesh with 5.1×10$^5$ triangular matrix*
846 *elements and 3.3×10$^4$ linear fracture elements; b) Aperture distribution derived from the*
847 *local stress state assuming sublinear length-aperture scaling relations with a maximum*
848 *horizontal stress oriented in the y-direction; c) Pressure gradient in the x-direction (indicated*
849 *by arrow) for a 1 mD matrix permeability; d) Fluid pressure in the y-direction.*

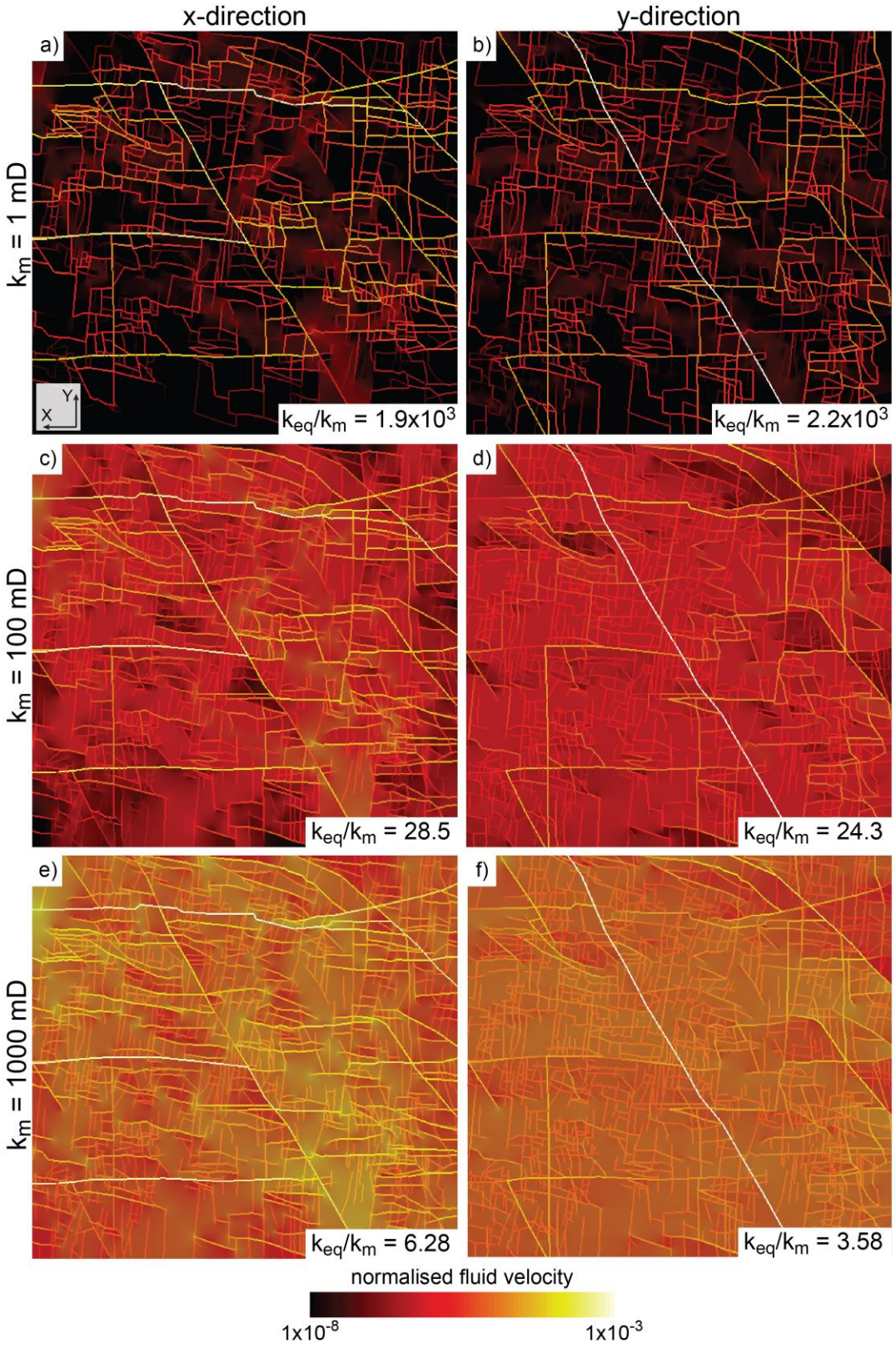


*Figure 15 Fluid velocity magnitudes under far-field pressure gradient in the x-direction (a, c, e) and y-direction (b, d, f) for different matrix permeabilities.*

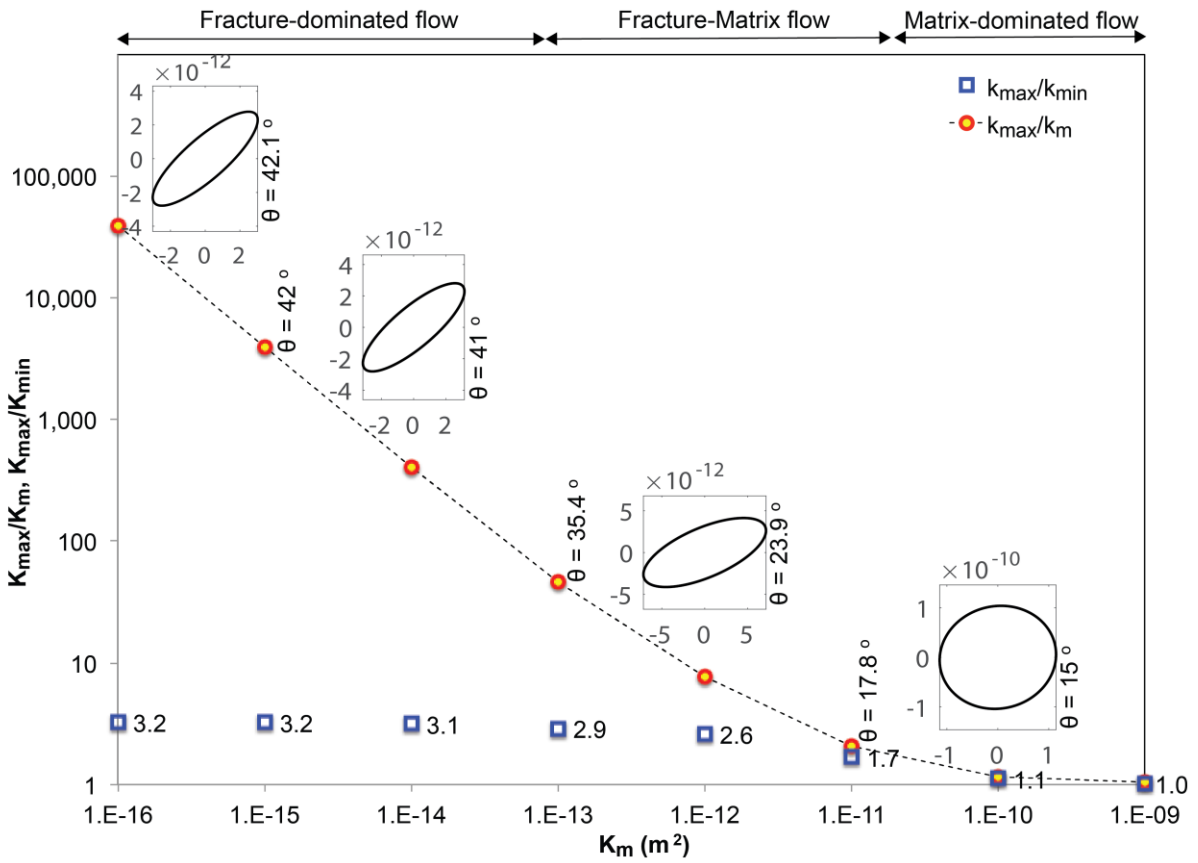


*Figure 16 Maximum permeability versus matrix permeability for a range of matrix permeabilities. The direction of maximum permeability is indicated by the ellipses and θ, measured from the East. The ratio between minimum and maximum permeability remains relatively constant except for Darcy-scale flow, where permeability is completely controlled by matrix flow.*